

Georg Urstöger, BSc

**Characterization of Proton Exchange
Membranes produced by Plasma
Enhanced Chemical Vapor Deposition**

Master Thesis

for obtaining the academic degree

Diplom-Ingenieur

Master Program of Technical Physics



Graz University of Technology

Supervisor: Dr. Anna Maria Coclite

Co-Supervisor: Ao.Univ.-Prof. Dipl.-Ing. Dr.techn. Roland Resel

Institute for Solid State Physics

Graz, February 2015

EIDESSTATTLICHE ERKLÄRUNG

AFFIDAVIT

Ich erkläre an Eides statt, dass ich die vorliegende Arbeit selbstständig verfasst, andere als die angegebenen Quellen/Hilfsmittel nicht benutzt, und die den benutzten Quellen wörtlich und inhaltlich entnommenen Stellen als solche kenntlich gemacht habe. Das in TUGRAZonline hochgeladene Textdokument ist mit der vorliegenden Masterarbeit/Diplomarbeit/Dissertation identisch.

I declare that I have authored this thesis independently, that I have not used other than the declared sources/resources, and that I have explicitly indicated all material which has been quoted either literally or by content from the sources used. The text document uploaded to TUGRAZonline is identical to the present master's thesis/diploma thesis/doctoral dissertation.

Datum / Date

Unterschrift / Signature

Acknowledgment

First and foremost, I would like to express my gratitude to my supervisor Anna Maria Coclite for supporting and teaching me throughout my thesis. Specifically the opportunity to attend the International Conference for thin films in Dubrovnik was a great opportunity for me. Also I want to thank my co-supervisor Roland Resel for his constructive input and his time for all of my many questions.

My special thanks are extended to all the people at the university that grew to be so much more than just colleagues, consisting of Roman Lassnig, Boris Scherwitzl, Stefan Pachmajer, Reinhold Hetzel and Katrin Unger. I enjoyed every discussion and am thankful to everyone of you for your moral support and scientific input.

I would also like to mention the whole group of friends that formed during my study, namely Paul Christian, Patrick Falk, Benjamin Lang, Gernot Kraberger, Christian Röthel, Christian Neubauer and Manuel Zingl. Without the numerous interesting and lively debates these years would not have been the same.

Here I would also like to thank Robert Schennach for his constant support with the FTIR spectroscopy and Bettina Friedel for her help with the profilometry. The assistance provided by Birgit Kunert, Elisabeth Stern and Harald Kerschbaumer was also greatly appreciated.

Acknowledgment

I especially want to thank my parents and my siblings for their unconditional support during the six years of my study and every experience they enabled me to have. And finally I want to thank my better half Bettina Unterberger for her great patience and her moral support during my thesis.

Abstract

In humanities journey on the way to clean, sustainable energy, many believe that the discovery and especially the immense improvement of fuel cells in the last century marked the onset of a new energy revolution. However there is still a great potential for improvement of the technology as for example in the electrodes and the electrolytes that are used. In this thesis we set out to produce a proton exchange membrane (PEM) that can compete with Nafion® (conductivity of ≈ 100 mS), the current benchmark for electrolytes. The method we chose to produce the films was plasma enhanced chemical vapor deposition (PECVD). To meet the working requirements of fuel cells these membranes are constructed to have hydrophilic groups from methacrylic acid (MAA) embedded in a structurally stable hydrophobic backbone from hexamethyldisiloxane (HMDSO). PECVD has the advantage that it produces generally homogeneous, crosslinked films that exhibit a good thermal stability and has no trouble combining monomers with different solubilities. However due to the randomness of the electronic fragmentations in plasma processes one needs to be careful not to destroy the molecules functionalities. We demonstrated that the effective power (through the Yasuda factor) can be used as the principal parameter affecting the behaviour of our system. It was shown that the parameters of the plasma process (comonomer ratio, plasma power, pressure) are correlated with the properties and the deposition rate of the film. The stability of the copolymers in water was

Abstract

investigated and showed that a longer stability can be obtained by depositing the films at a lower pressure or by decreasing the amount of hydrophilic groups from MAA in the film. The proton conductivity measurements were performed with electrochemical impedance spectroscopy and showed that for the stable films a conductivity of 1.1 mS is obtained.

Kurzfassung

Auf dem Weg der Menschheit zu sauberen, nachhaltigen Energiequellen glauben viele, dass die Entdeckung und vor allem der immense Fortschritt in der Entwicklung von Brennstoffzellen im letzten Jahrhundert den Beginn einer Revolution der Energieerzeugung markieren. Dennoch existiert noch viel Potential diese Technologie zu verbessern, zum Beispiel in der Verwendung der Elektroden oder des Elektrolyten. Das Ziel dieser Arbeit ist es Protonen leitende Membranen (PEM) zu produzieren, welche mit dem gängigen Maßstab Nafion® (Leitfähigkeit von $\approx 100 \text{ mS}$), konkurrieren können. Die Produktionsmethode für unsere Filme war die der plasmaunterstützten chemische Gasphasenabscheidung (PECVD). Um den Arbeitsbedingungen einer Brennstoffzelle zu genügen bestehen die Membranen aus hydrophilen Gruppen von Methacrylsäure (MAA) welche in einer strukturell stabilen hydrophoben Matrix aus Hexamethyldisiloxane (HMDSO) eingebettet sind. PECVD hat den Vorteil, dass es grundsätzlich homogene, quer vernetzte Filme mit guter thermischer Stabilität erzeugt. Ebenfalls erlaubt diese Methode Monomere mit verschiedenen Löslichkeiten zu kombinieren. Allerdings muss wegen der Zufälligkeit der durch Elektronen verursachten Fragmentation darauf geachtet werden, dass die Funktionalität der Monomere nicht zerstört wird. In dieser Arbeit konnte demonstriert werden, dass die effektive Leistung (gegeben durch den Yasuda Faktor) als grundsätzlicher Parameter herangezogen werden kann um das Verhalten

Kurzfassung

unseres Systems zu beschreiben. Es konnte gezeigt werden, dass die Parameter des Plasma Prozesses (Komonomer Verhältnis, Plasma Leistung, Druck) mit den Eigenschaften und der Depositionsrate der Filme korrelieren. Die Stabilität der Filme in Wasser wurde untersucht und es konnte gezeigt werden, dass die Stabilität erhöht werden kann wenn die Filme bei niedrigerem Druck hergestellt werden oder wenn weniger hydrophile MAA Gruppen in dem Film eingebunden werden. Die Protonenleitfähigkeit wurde mittels Elektrochemischer Impedanz Spektroskopie (EIS) untersucht und ergab für die wasserstabilen Filme eine Leitfähigkeit von 1.1 mS.

Contents

Acknowledgment	v
Abstract	vii
Kurzfassung	ix
1 Introduction	1
2 Fundamentals	3
2.1 Fuel Cell	3
2.1.1 Working Principle	4
2.1.2 Efficiency of a Fuel Cell	7
2.2 Proton Exchange Membrane (PEM)	8
2.2.1 Proton Conductivity	8
2.2.2 Properties of Membranes	10
2.2.3 Types of PEMs	13
2.3 Plasma enhanced chemical vapor deposition (PECVD)	14
2.3.1 Plasma deposition process	15
2.3.2 The Yasuda Factor	19
2.3.3 The influence of pressure and inert gases	19

Contents

3	Experimental	21
3.1	Molecules	21
3.2	Reactor setup	23
3.3	Film Analysis	25
3.3.1	Fourier Transform Infrared Spectroscopy (FTIR)	25
3.3.2	X-Ray-Reflectivity (XRR)	27
3.3.3	Profilometry	30
3.3.4	Water Contact Angle Measurement	31
3.3.5	Electrochemical Impedance Spectroscopy (EIS)	33
3.4	Reactor set-up	35
4	Results and Discussion	39
4.1	Homopolymers	39
4.1.1	Pure Hexamethyldisiloxane (HMDSO)	39
4.1.2	Pure Methacrylic Acid (MAA)	42
4.2	Copolymers	46
4.2.1	Copolymer of constant HMDSO and varying MAA	46
4.2.2	Copolymer of constant MAA and varying HMDSO	48
4.2.3	Variation of the total flow rate with a constant ratio	52
4.2.4	Variation of argon flow rate at a constant flow of monomers	55
4.2.5	Variation of power at a constant flow of monomers and argon	58
4.2.6	Variation of pressure at constant flow rates	62
4.2.7	Copolymer at constant HMDSO and varying MAA	66
5	Conclusion	71
	Bibliography	73

1 Introduction

With the energy consumption of the world being as large as ever and a runaway greenhouse effect on our doorstep the need for more efficient and healthier technologies is one of our planets most urgent goals. In that sense converting energy with a process that uses the most common element in the universe and creates water as a waste product almost sounds too good to be true. Yet this is exactly what fuel cells are capable of doing. The first observation of a fuel cell effect was made 1838 by Christian F. Schoenbein. Shortly after in 1839 Sir William Grove demonstrated the first fuel cell which he called "gaseous voltaic battery". After these findings it took more than 100 years for the first practical device to be built and it was not before the Gemini U.S. space program in 1960 that fuel cells were actually used. Although they continued to being used in the space program fuel cells were not of interest for terrestrial applications until the early 1990s. Most of the car companies picked up on this technology and by the end of the century built and demonstrated a fuel cell powered vehicle. At this point Japan, where fuel cell cars and warm water heating systems are already being commercially sold, and the United States show great interest in this technology. [1] Unfortunately due to expensive materials and complex production processes fuel cells have not yet succeeded in establishing themselves against technologies that currently dominate the market.

This high cost is one point we were trying to challenge in this work. The

1 Introduction

thesis concentrates on the proton conductive membrane that forms the heart of every fuel cell. The goal is to synthesize a product that incorporates a high proton conductivity with a good structural stability which should lead to a long lifetime of the membrane. To achieve this objective we made use of plasma enhanced chemical vapor deposition to combine the functionalities of different molecules and deposit them to form a homogeneous, stable thin film.

2 Fundamentals

2.1 Fuel Cell

A fuel cell works as an energy converter that transforms energy stored in hydrogen to electrical energy which then can be used to supply devices.

A good reference on this topic is the book "PEM Fuel Cells Theory and Practice" by Frano Barbir.¹ There are numerous reasons why it is useful or maybe even necessary to expand the research for these devices and here I would like to mention some of them.

1. The energy efficiency of fuel cells is very high ($\eta = 94.5\%$) compared to the internal combustion engine of cars ($\eta = 30\%$). η will be calculated in section 2.1.2.
2. Fuel cells, running on hydrogen as a fuel, generally produce water as a waste product and tend to emit low to zero concentrations of greenhouse gases.
3. Because of its simplicity the fuel cell has the potential of being produced at a very low cost. Unfortunately at this point the cost is still high due to the usage of expensive materials such as platinum for electrodes or Nafion® as membranes.
4. Fuel Cells are small. This makes them very useful for all sorts of applications such as cars, spacecrafts, bikes, heating units for water or even

2 Fundamentals

laptops.

There are different types of fuel cells such as Solid Oxide Fuel Cells, Alkaline Fuel Cells or Phosphoric Acid Fuel cells but here I will explain the working principle of **Polymer Electrolyte Membrane** or **Proton Exchange Membrane Fuel Cells (PEMFCs)**.

Due to all the advantages listed above fuel cells have countless possible applications. The largest two fields are transportation and stationary power. Both fields impose different requirements on the fuel cell for example in terms of power output, size or noise level. Today the majority of car manufacturers have produced a fuel cell prototype and on the 15. of December 2014 Toyota will introduce one of the first commercially available cars powered by fuel cell technology². Stationary household fuel cell applications are being sold since 2012.

2.1.1 Working Principle

A schematic of a fuel cell can be seen in figure 2.1 The two essential parts that form the main piece of every fuel cell are the electrodes and the electrolyte which separates the two electrodes. On the interface between the electrodes and the electrolyte there is a thin layer which acts as a catalyst. The two electrodes are connected by an external circuit which enables the electrons to generate electrical power. The underlying reaction that takes place is a redox reaction.

On the anode side the following reaction takes place



With H_2 being the hydrogen molecule, H^+ a proton and e^- an electron. The negative anode side is supplied with hydrogen that, once it comes in

2.1 Fuel Cell

contact to the catalyst layer, dissociates and subsequently oxidizes into its primary components, protons and electrons. The electrons are guided through an external circuit while the protons take their path through the membrane.

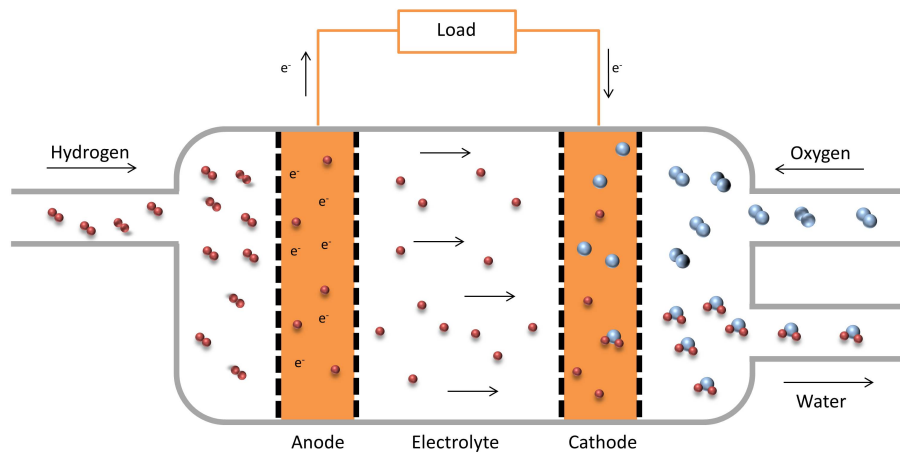
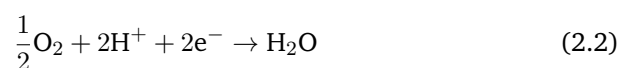


Figure 2.1: Schematic of a PEMFC. Hydrogen is delivered to the membrane and split up into protons and electrons. The protons diffuse through the electrolyte layer while electrons move over an external circuit. At the cathode side all species combine together with oxygen and form water.

While on the cathode side:



O_2 being oxygen and H_2O water. When oxygen touches the catalyst layer between the cathode and the electrolyte it also first dissociates and then reduces with the surplus of the electrons. In a final step the reduced oxygen picks up two protons and forms water.

2 Fundamentals

These two reactions can be combined to an overall reaction



This means that as a waste product the fuel cell produces water and heat. Both need to be handled to ensure the performance but in some cases might also be of use (e.g. warm water heater).

The **electrolyte** forms the heart of the fuel cell. Since it is the main focus of this thesis it will be covered in more detail in section 2.2.

The **electrodes** typically have two main requirements to fulfill

1. They need to be good electrical conductors to ensure that the electrons reach the external circuit with as little losses as possible.
2. They have to be catalysts to trigger the chemical reactions.

Therefore electrodes for fuel cells are typically made of a layer of platinum. Platinum is a very expensive metal and one reason why fuel cells today are still costly compared to other devices.

Apart from the electrodes and electrolyte there are also gas diffusion layers and bipolar plates.

The platinum layer is usually deposited on a porous carbon substrate which act as a **gas diffusion layer**. As the name suggests its main purpose is to deliver the reactive gases to the catalyst layer. Among other functions it also needs to act as a channel to guide the excess water out of the fuel cell.

Finally the gas diffusion layer is deposited on the **bipolar plates** that acts as a collector for electrons and connects the anode to the cathode. These three parts are usually talked about as the Membrane Electrolyte Assembly (MEA).

2.1.2 Efficiency of a Fuel Cell

The efficiency can be calculated by the ratio of useful energy output and the energy input.

$$\eta = \frac{\Delta G}{\Delta H} \quad (2.4)$$

ΔH being the change in enthalpy and ΔG the change in the Gibbs free energy.

ΔH can be calculated easily by the difference of the individual formation enthalpies in equation 2.3. From literature we find that the formation enthalpy of water is $h_{\text{H}_2\text{O}}^f = -286 \text{ kJ mol}^{-1}$ at 25°C . The enthalpy of formation of elements is by definition zero.

Therefore we can now calculate the change in enthalpy to

$$\begin{aligned} \Delta H &= h_{\text{H}_2\text{O}}^f - h_{\text{H}_2}^f - \frac{1}{2}h_{\text{O}_2}^f \\ &= -286 \text{ kJmol}^{-1} \end{aligned}$$

This is the heat that is produced by reaction 2.3. Since every reaction always produces entropy not all of the produced heat can be converted to electricity. The maximum energy that can be used to generate electrical power corresponds to the Gibbs free energy. It is given by

$$\Delta G = \Delta H - T\Delta S \quad (2.5)$$

In other words the Gibbs free energy includes the losses due to the generation of entropy. With the values for the entropies of the specific products and reactants given by literature, ΔS can be calculated similar to ΔH with Equation 2.3.

2 Fundamentals

$$\begin{aligned}\Delta S &= s_{\text{H}_2\text{O}}^f - s_{\text{H}_2}^f - \frac{1}{2}s_{\text{O}_2}^f \\ &= -0.1633 \text{ kJmol}^{-1}\text{K}^{-1}\end{aligned}$$

This means that (at 25 °C) we obtain for the change in Gibbs free energy a value of $\Delta G = -237.34 \text{ kJmol}^{-1}$. And with this result we can finally calculate the theoretical efficiency of a fuel cell with equation 2.4 to

$$\eta = 83 \% \quad (2.6)$$

This high efficiency is one of the major reasons why the commercialization of fuel cells would be of great advantage for all of us. In the introduction part of this chapter I mentioned an efficiency of 94.5%. It depends on how you calculate the efficiency. Usually the efficiency of energy conversion devices is calculated with the higher heating value of the fuel (as did I in this section). The efficiency of the internal combustion engine on the other hand has traditionally been calculated with the lower heating value and since I compared the two conversion devices I used the lower heating value for fuel cells to get a stronger and more accurate contrast.

2.2 Proton Exchange Membrane (PEM)

2.2.1 Proton Conductivity

Proton conductivity is generally described as an interplay of two mechanisms. One mechanism is the diffusion driven vehicular mechanism the other one is called Grotthuss "hopping" mechanism. Both mechanism explain the conduction of protons through interaction with water molecules. The vehicular mechanism

2.2 Proton Exchange Membrane (PEM)

suggests that a proton attaches to a water molecule forming hydronium H_3O^+ and diffuses through the water. This mechanism transports not only the proton but also water which leads to the effect of electroosmotic drag.

The Grotthuss mechanism suggests that protons can hop along a chain of water molecules jumping between different states of solution such as Zundel (H_5O_2^+) or Eigen (H_9O_4^+) Ions. It is generally assumed that this mechanism has to be accompanied by some sort of structural reorientation as paths taken by the proton end up in an electrostatically unfavorable position for new protons to hop. This mechanism is often referred to as "structural diffusion" since the transport of the proton involves the movement of hydrogen-bond breaking and formation processes. A schematic of the mechanism can be seen in figure 2.2.³

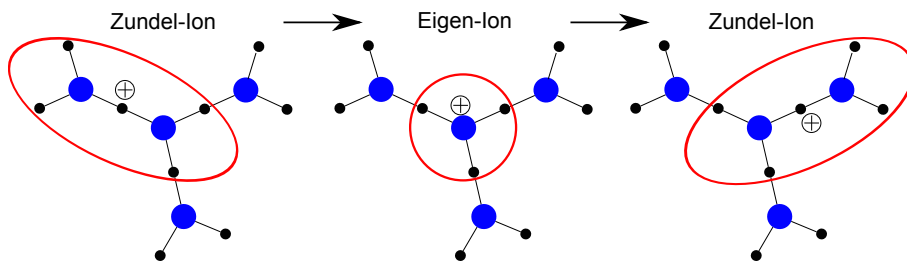


Figure 2.2: Schematic of the Grotthuss mechanism. The proton hops between different states of solution. This is one mechanism how a proton can migrate in a network of water molecules. Driven by a gradient in the chemical potential the proton jumps between being shared by two water molecules (Zundel-Ion) and being attached to one water (hydronium) surrounded by three water molecules (Eigen-Ion). To trigger the interchange between these two states a more extended network needs to be considered that involves also the formation and breaking of hydrogen bonds and can be found in [3].

The addition of acids has been generally described to enhance proton con-

2 Fundamentals

ductivity by adding more protons to the system and by providing sites for hydrogen- and ionic bonds to which the proton can hop. However there has also been documentation of a negative effect since the negative ends of acids (once the proton is dissolved) attract positive charges and therefore disrupt the proton conduction. This seems to depend on the hydration level of the structure. At a certain number of water molecules per acid group the positive proton is fully screened from the negative charge of the acid group which affects the proton conductivity. A schematic on how the proton conduction mechanisms work in a membrane is shown in figure 2.3 [3–5].

Immersed in water Nafion® was described to be forming ionic channels through which the protons move. These channels, that are also very stable within the strong hydrophobic backbone, are the reason why Nafion® has such a high proton conductivity ($S = 104 \frac{mS}{cm}$). [3, 6] It has been described in literature that the domination of one mechanism over the other depends on the hydration level of the membrane but also on other parameters such as temperature, amount of acid groups or pressure. [3, 7, 8]

2.2.2 Properties of Membranes

As aforementioned, PEMs form the heart of every fuel cell and need to satisfy many requirements. First and most importantly of all it needs to be proton conductive. As water increases the proton conductivity (explained in section 2.2.1) the membrane needs to have a certain water uptake, in other words "swellability", to work efficiently. On the other hand as the water content increases the membrane still has to maintain their structural stability. In other words we want to construct a membrane with a **hydrophobic** backbone to ensure the stability and a **hydrophilic** structure attached to this backbone to

2.2 Proton Exchange Membrane (PEM)

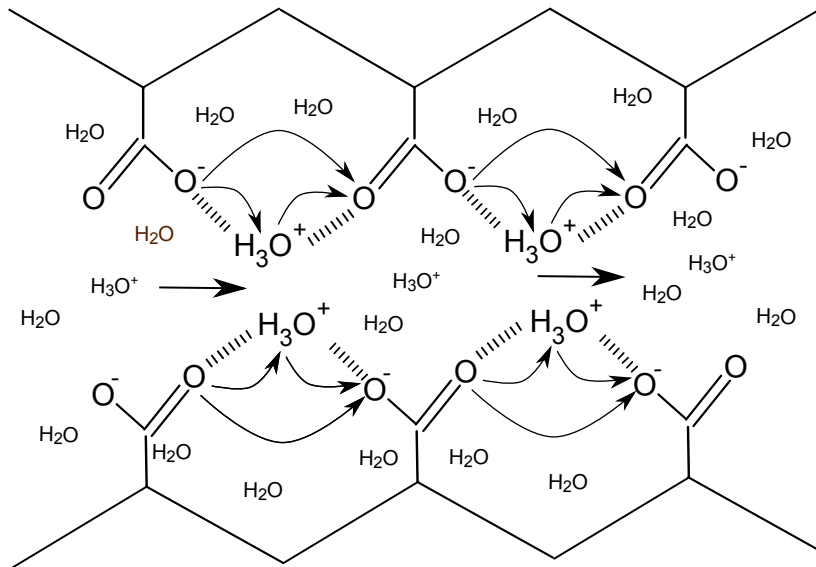


Figure 2.3: Illustration of the proton conduction in a PEM. Usually both mechanisms, Grotthuss and vehicular, contribute to the proton conduction. For proton conduction it is favorable that the water accumulates at the acid groups to form ionic channels within the hydrophobic backbone.

serve as proton transport channels. As a image to visualize these properties one can think of a membrane as of a microscopic sponge. The swelling behavior is illustrated in figure 2.4.

The structure of Nafion® can be seen in figure 2.5. The membrane combines the hydrophobic structure of Teflon ($[\text{CF}_2\text{-CF}_2]_n$) with the hydrophilic properties of SO_3H . It is the combination of these two groups that enables Nafion® to exhibit a high proton conductivity of $90 - 120 \frac{\text{mS}}{\text{cm}}$ while obtaining an excellent lifetime of up to 4000 hours. [7]

Additionally to these properties the membranes should be perfectly insu-

2 Fundamentals

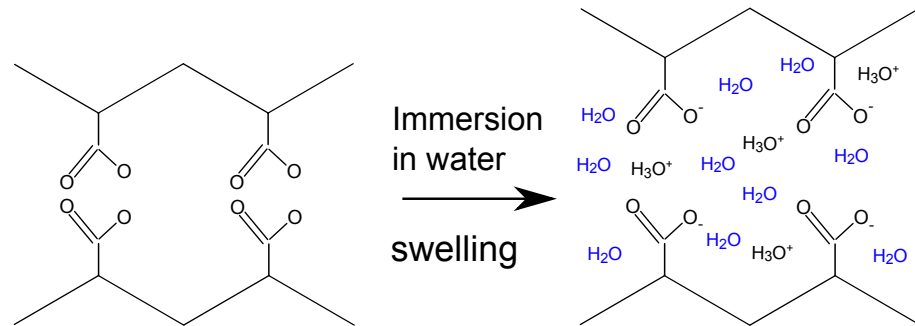


Figure 2.4: Schematic to visualize membrane properties. The membrane absorbs water and therefore increases in thickness because of its hydrophilic structure. Ideally this increase in thickness is accompanied by the formation of an ionic channel.

lating for electrons and should be impermeable for reactive gases as it would lower the efficiency. Also since the operating temperatures are often elevated the structure should be stable up to 80 °C.

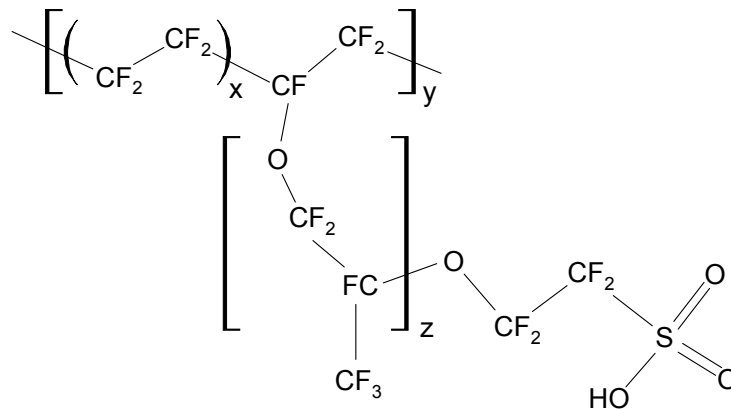


Figure 2.5: Chemical structure of Nafion®. Different values for x,y and z determine the structure and properties of the material. [9]

2.2.3 Types of PEMs

Generally proton exchange membranes can be classified into three groups.

1. **Perfluorinated ionomers (or partially perfluorinated):** These are membranes that incorporate the fluorine atom because of its high electronegativity. For proton conduction, acid groups, such as SO_3H , are added to the polymer. Nafion® being produced from a perfluorosulfonic acid belongs to this group. The advantages of these PEMs are high proton conductivity, good thermal stability and good mechanical strength.
2. **Non-fluorinated hydrocarbons:** As the name suggests this type of membrane does not use fluorine for their backbone. Instead they consist of aliphatic or aromatic hydrocarbons combined with polar side groups. The big advantage over fluorinated membranes is that they are less expensive. Apart from that the simple hydrocarbon structure makes it easy to introduce polar groups to the polymer increasing the proton conductivity. Such polymers show high water uptake. The copolymer we are trying to produce would be categorized as one of this group.
3. **Acid-base blends:** Usually these sort of membranes are produced by adding an acidic component to an alkaline polymer base. In these materials humidification is not needed to provide the proton conductivity. The ionic cross-linking and hydrogen bonding between the acidic and alkaline parts of the polymers allows the control of swellability while maintaining the flexibility. A prominent membrane of this type is sulfonated poly(etheretherketone) (sPEEK). [8],[10]

2.3 Plasma enhanced chemical vapor deposition (PECVD)

This section follows chapter nine of the book "Handbook of deposition technologies for films and coatings: science, applications and technology" and the book "Plasma processing of polymers. [11, 12]

Chemical vapor deposition (CVD) is one of many techniques to deposit thin films on various kind of substrates. In this technique precursor molecules are influenced, by different processes (Oxidation, thermal activation, electron collision), in such a way that they become chemically reactive and subsequently undergo reactions on the surface of the substrate and chemisorb, forming thin films. This presence of chemical binding reactions on the surface is the major difference to physical vapor deposition. [13]

Plasma is an electrically neutral state of matter in which the electrons are partially (or fully) separated from their nuclei. The processes occurring in a plasma are complex as they are but when functional monomers are introduced to the plasma the diversity of species and interactions increases even further. Depending on the energy introduced to our system these species can exist in different levels of excitation.

A plasma can be ignited applying an alternating current (AC) electric field to the gas. The electrons will start to oscillate in that field and gain more energy during every cycle. The particles start colliding with other species and if enough energy is supplied the atoms will eventually ionize. Recombination of electrons and nuclei under emission of a photon can be observed and plasmas of this kind are known under the term **glow discharge**. At low pressures the electrons collide not frequently enough to fully distribute the temperature over the whole system and all the species. Therefore at low pressures plasmas will typically not

2.3 Plasma enhanced chemical vapor deposition (PECVD)

exceed temperatures above 100 °C and are referred to as **cold plasma**.

Usually the PECVD systems consist of a reaction chamber, a pumping system, the power supply, a matching network and the instruments to measure and vary parameters such as the working pressure or the flow rate of monomers and gases. The most common used setups are parallel plate reactors which can be supplied with low, medium or radio frequency (RF) power. Other methods use for example microwave or thermal techniques to ignite the plasma. The setup used in this work will be covered in the experimental part of the thesis.

At frequencies above 1 MHz the ions are unable to follow the electric field which means that only electrons are influenced. At low pressures this means that the electrons continue to be the most energetic species. The electrons which are lighter and therefore more mobile than the ions charge every isolated surface negatively with respect to the plasma. As these surfaces get charged negatively electrons and negative ions are repelled which leads to the phenomena described in literature as **plasma sheath**. On the other hand positive ions are attracted and accelerated towards these surfaces leading to an effect called **ion bombardment**, which will play an important role in the deposition process.

2.3.1 Plasma deposition process

As the plasma is ignited and the electrons start transferring energy by elastic and inelastic scattering, other species are excited, ionized or even fragmented. As mentioned earlier there are many interactions that can occur with some being explained in detail below. A list of all the possible interactions can be found in the literature cited in this thesis. However the interactions in a plasma can be categorized in two groups.

Plasma Gas-Phase Reaction

2 Fundamentals

As mentioned, electron collisions can lead to ionization, excitation or dissociation of atoms and molecules. While on the one side ionization sustains the plasma, exciting and dissociative processes create reactive species which leads to the desired plasma polymerization. For PECVD the dissociation process is the most important one. If a colliding electron has more energy than a specific bond energy of the molecule the bond breaks and two radicals are formed as schematically shown in figure 2.6.



These radicals have now numerous possibilities to react in the system. Further electron collisions could lead to another dissociation of the radical. Or the radical could combine with other species to form a new radical or could form a stable molecule such as $\text{CH}_3 + \text{H} \rightarrow \text{CH}_4$. In the case that it forms a stable molecule it could end up being pumped off into the pump but can also undergo re-dissociation. When the radicals formed in the gas phase come close to the surface they **physisorb** onto it as in figure 2.6.



With R being a radical and R_{ads} the physisorbed radical.

Plasma-Surface Reactions

The plasma sheath that forms at isolated surfaces has the consequence that these surfaces get subsequently bombarded with ions. These collisions create activated sites on the surface. In other words it creates free dangling bonds that stick out of the surface. The reactions for plasma-surface interactions are shown in figure 2.7.



2.3 Plasma enhanced chemical vapor deposition (PECVD)

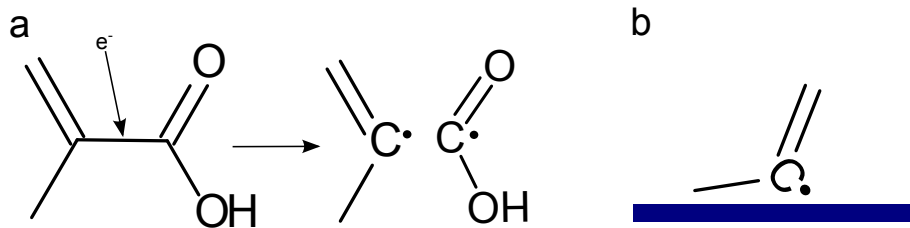


Figure 2.6: Schematic of plasma-gas-phase reactions. a) shows the formation of a radical by the collision of the monomer with an electron. b) The radicals formed in the gas-phase physisorb on the surface.

with S being the surface and $(S-\cdot)^*$ the activated surface site with a free bond. At low pressures where collisions between ions and gas particles are rare, the energy of the ions will be the difference between the cathode potential and the plasma potential. At higher pressures the ions collide more often and the average bombardment energy will be less than the drop of the potential across the sheath. Ions striking the surface have great impact on the chemical composition of the film and influences the adsorption of molecules.

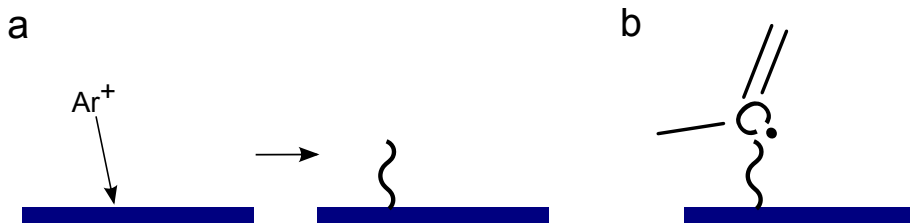


Figure 2.7: Graphic to illustrate plasma-surface reactions. a) Surface activation by ion bombardment. b) Chemisorbtion of a radical by combination of a migrating physisorbed radical and an activated surface site.

Although ions are accelerated towards the surface the electrons will be

2 Fundamentals

slowed down. This means that generally electrons will hit the surface at relatively low energies leading to surface heating. However electrons can also alter the chemical composition of the film by exciting or ionizing surface species that can lead to rearrangement of bonds, dissociation or even desorption.

In the last step the thermally activated surface migration of physisorbed radicals from step 2.10 find one of the activated surface sites and chemically binds to it as illustrated in figure 2.7.



The deposited film now forms the new surface and the processes from steps 2.7 - 2.10 are repeated. This model of surface growth is known as the Activation Growth Model (AGM). [14–19] Due to the many different processes during plasma polymerization the resulting film will usually be of an amorphous nature without a constant repeating monomer unit as illustrated in figure 2.8.

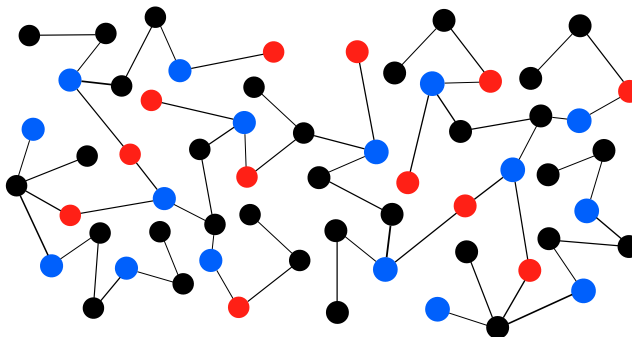


Figure 2.8: Illustration of an amorphous network produced by PECVD

2.3 Plasma enhanced chemical vapor deposition (PECVD)

2.3.2 The Yasuda Factor

In the 70s H. Yasuda et al. [20] suggested a new approach to describe the processes during plasma polymerization. They argued that instead of using the pressure or the power as sole parameters, the effects can be described more accurately by introducing an effective power, namely the Yasuda factor.

$$W_{\text{eff}} = \frac{W}{F \cdot M} \quad (2.11)$$

With W being the applied power, F the flow rate of the monomer and M the molecular weight of the monomer. This factor describes the effective power per unit mass of monomer. The Yasuda factor influences chemistry obtained by the deposition in different ways. As we increase the flow rate of monomers the effective power decreases and might fall under some critical value to sustain the plasma or to fragment the monomers. Also for monomers with different molecular weights the effective power changes and might show lower deposition rates. However this also depends on the specific bond energies and chemical structure of the monomers used. The assumption is that if one applies a high effective power per molecule it is likely that most of the molecules will be fragmented and will therefore lose some of their functionality. However a high fragmentation usually is favorable for a highly crosslinked network. On the other hand a low effective power will retain the structure of the monomers and will have a tendency for oligomerization which usually reduces the crosslinking.

2.3.3 The influence of pressure and inert gases

Pressure has two main effects. First it influences the density of particles and subsequently the mean free path. This means that at lower pressures the average number of collisions is low. The species can travel farther before they exchange

2 Fundamentals

their energies by collisions and therefore the active plasma zone can extend farther into the reactor. The behavior is schematically shown in figure 2.9. As a result of the lower pressure the plasma sheath also becomes larger which leads together with the longer mean free path to a more intense ion bombardment of the sample. [11, 21]

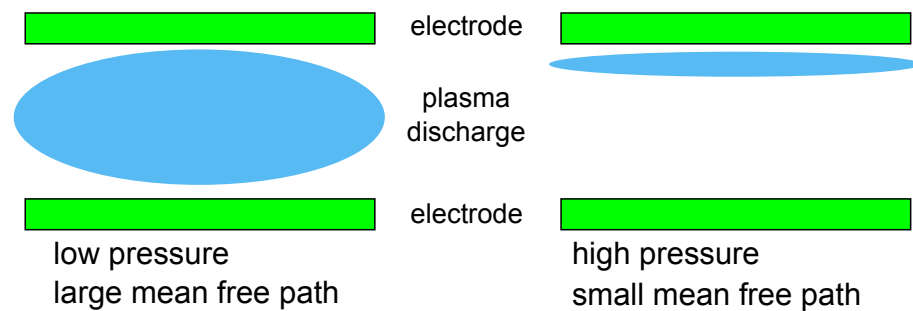


Figure 2.9: Influence of pressure on the plasma discharge. At low pressure the glow discharge extends farther into the reactor whereas at high pressures it is confined to the top electrode.

Inert gases are often added to the discharge to enhance the stability and homogeneity of the plasma and to increase the number of active colliding species. However it has been reported in literature that the addition of inert gas such as argon up to a certain ratio show no effect on the deposition rate nor on the film properties. The method they used to consider the flow of argon was to introduce a factor so that the argon does not fully contribute to the flow rate $F = F_M + a \cdot F_g$. From data values between 0.05 and 0.1 have been derived for argon [22].

3 Experimental

The purpose of this thesis was to produce proton conducting membranes by plasma enhanced chemical vapor deposition. However setting up the reactor turned out to be more problematic than expected. The discussion of these problems is covered in section 3.4. The analysis of the films was carried out by x-ray reflectivity, Fourier transform infrared spectroscopy, profilometry, water contact angle and impedance spectroscopy.

3.1 Molecules

The molecules we use to produce our films are hexamethyldisiloxane (HMDSO) and methacrylic acid (MAA). The chemical structure can be seen in figure 3.1. The HMDSO and the MAA are used to create a hydrophobic backbone and the hydrophilic ionic channels, respectively. The properties of the molecules can be seen in table 3.1. From this table we can see that the HMDSO is a more volatile substance than the MAA which will have an influence on how we set up our reactor.

As one can see in figure 3.1 the HMDSO has many CH_3 groups. By incorporating these non-polar hydrophobic groups we want to be able to tune the hydrophobicity of our copolymer. The MAA on the other hand has a polar COOH group which, embedded in the hydrophobic matrix, should lead to ionic conduc-

3 Experimental

Table 3.1: Properties of Molecules. Obtained from the Material safety data sheet of Sigma Aldrich.

	Molecular Weight / $\text{g} \cdot \text{mol}^{-1}$	Boiling Point / $^{\circ}\text{C}$	Vapor Pressure at 20°C / hPa
HMDSO	162.38	101	20
MAA	86.09	163	1

tivity and ideally form ionic channels. In table 3.2 the average binding energies of the bonds of these molecules are listed. From these average binding energies one can see which bonds are more likely to be broken than others. This can give you an idea how the copolymers will change when we vary the deposition parameters and it will serve us to explain the behavior to some extent.

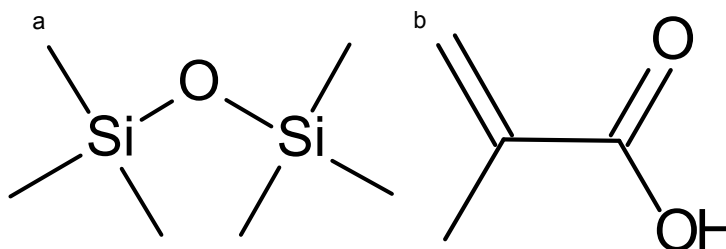


Figure 3.1: a) Hexamethyldisiloxane (HMDSO). Due to the many CH_3 groups the idea is to get a hydrophobic backbone from this molecule. b) Methacrylic acid (MAA). The carboxylic acid (COOH) is hydrophilic and used to enhance the proton conductivity.

Table 3.2: Average binding energies of the specific bonds of the molecules [23].

HMDSO		MAA	
Bond	Bond Energy / kJmol^{-1}	Bond	Bond Energy / kJmol^{-1}
O-Si	444	C=O	708
C-H	416	O-H	463
Si-C	306	C-O	358
		C-C	345

3.2 Reactor setup

The plasma reactor can be seen in figure 3.2. The vacuum system consists of a rotary vane pump (Duo 5M) and a turbo drag pump (TMH 071 P). The pumps are connected in such a way that the rotary pump is either connect directly to the system or through the turbo pump and a butterfly valve (MKS Type 253B) to the reaction chamber. The base pressure of ≈ 9.5 mTorr is reached after an evacuation time of ≈ 20 min. However the evacuation time increases with the number of depositions. Usually we obtained leak rates in the range between 0.01 – 0.1 sccm but this depends on the time the chamber was evacuated as more and more residue of the monomers desorb. The unit sccm stands for standard cubic centimeters per minute and gives the amount of volume that passes through a given point within one minute of time. Standard conditions in this case means 0°C and 1013.25 mbar.

The RF-Power for this asymmetric parallel plate reactor is supplied by a Cesar 136 RF Power Generator (13.56 MHz and 275 V) via an appropriate matching network to the electrode from the top. The electrode was chosen to be in a shower head configuration which should lead to a more homogeneous distribu-

3 Experimental

tion of monomer. Since the reactor is grounded the top electrode was installed on an isolating structure which is drawn in green in figure 3.2.

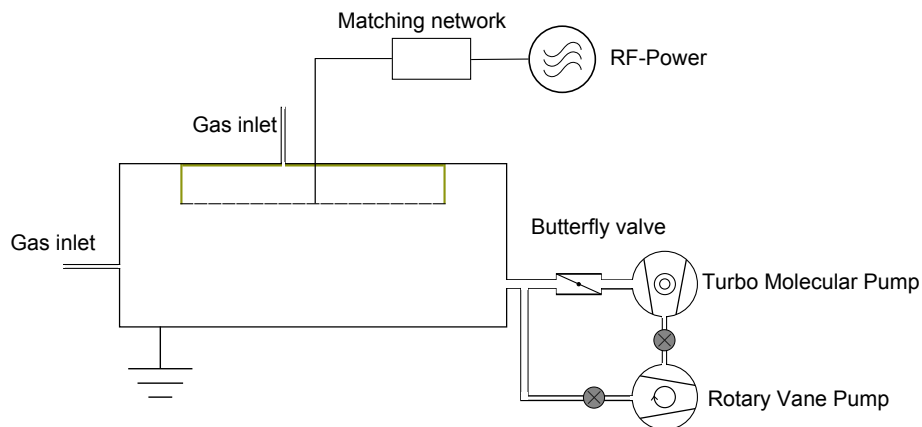


Figure 3.2: Schematic of the plasma deposition reactor used in this thesis.

The reactor has two gas inlets. One from the top through the shower head configuration and one from a connection at the side. The volatile gases are introduced from the top through the shower head and the non-volatile monomer from the side. The monomers are thermally vaporized and flow over a connection line into the chamber. To vaporize the non-volatile monomer, it is heated up to 70 °C and the line is heated to 100 °C. Omega Temperature controller (CN 2110) are used together with heating tapes to keep the temperature constant. To control the flow rates needle valves were installed in the monomer lines.

The pressure in the reactor is measured by a gas independent MKS-Baratron 626 gauge and is controlled by the butterfly valve. In figure 3.3 one can see the actual setup of the reactor.

3.3 Film Analysis

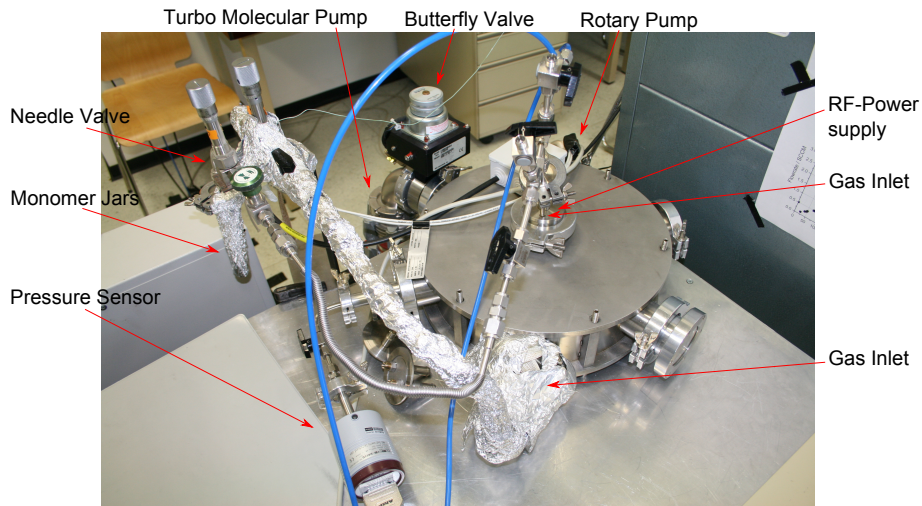


Figure 3.3: Plasma enhanced chemical vapor deposition reactor.

3.3 Film Analysis

In this section I will briefly explain the methods I used to analyze my samples.

3.3.1 Fourier Transform Infrared Spectroscopy (FTIR)

FTIR was used to investigate the chemical composition of our copolymers. In IR spectroscopy infrared light is used to excite vibrational modes of the molecules. The energy at which excitation absorbs the incoming light is determined by the strength of the bond and the masses of the contributing atoms or in quantum mechanical words the energy gap that needs to be overcome to excite the bond. The intensity of the peaks however is determined by the change of the dipole moment and the amount of bonds that are available at this energy. [24]

The spectrometer used is a Bruker IFS 66 V Fourier transform infrared

3 Experimental

spectrometer. One advantage of the setup is the feature to evacuate the complete system which increases the intensity of the incoming light. The samples are measured in transmission mode and to minimize influences of the substrate a reference was recorded immediately after each measurement. The detector is a Mercury Cadmium Telluride (MCT) semiconductor detector. For comparison every thin film was normalized by their thickness. In general it is better to measure samples that are thicker than ≈ 200 nm as with increasing thickness one obtains a better signal. The open apparatus can be seen in figure 3.4.



Figure 3.4: Bruker IFS 66 V Fourier transform infrared spectrometer.

In figure 3.5 one can see an exemplary measurement of a copolymer I produced. The important bonds have been labeled for a better oversight. Some of the absorptions can only come from one of the molecules such as in the case of the C=O bond at 1700 cm^{-1} which can only come from the carboxylic acid in MAA. This makes it easy to determine whether we obtain more or less of these

3.3 Film Analysis

functional groups in our polymer. In table 3.3 characteristic excitations of the molecules are listed.

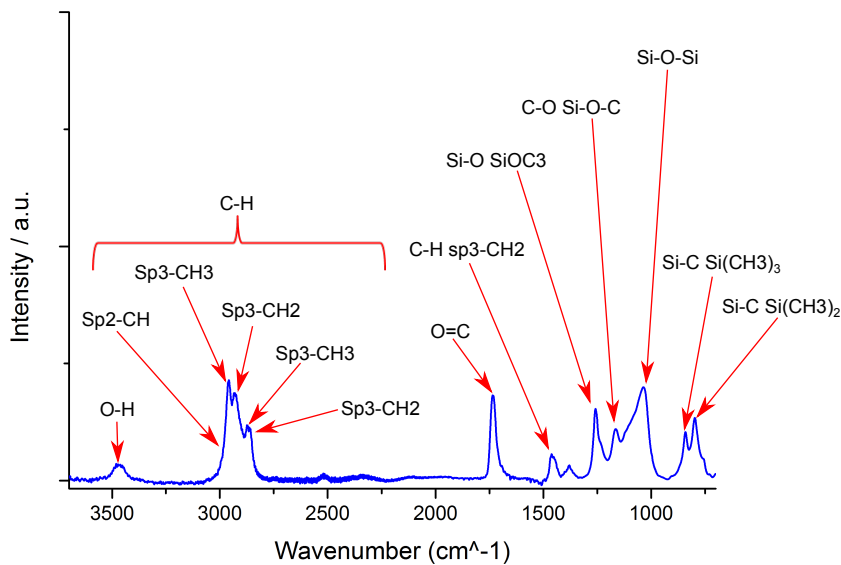


Figure 3.5: Example of an interferogram of a film of MAA and HMDSO. The C-H Sp³ oscillations at 3000 cm⁻¹ consist of an asymmetric stretching and a symmetric stretching part which explains why they appear twice.

3.3.2 X-Ray-Reflectivity (XRR)

XRR was mainly used to determine the thickness of our films. The device used is a Panalytical Empyrean X-Ray diffractometer with a Pixel 3D detector. The samples are measured in a standard specular scan with the main difference to x-ray diffraction being the smaller scanning range (1 – 7°) and the smaller

3 Experimental

Table 3.3: Characteristic absorption lines for MAA and HMDSO. [25–27]

Absorption Range / cm^{-1}	Bond and group	Vibrating Mode
3500 - 3400	O-H in H_2O	asym. stretch
3400 - 3000	O-H in COOH	asym. stretch
3000 - 2800	C-H in CH_2 , CH_3	asym. and sym. stretch
1735	C=O in COOR	stretch
1705	C=O in COOH	stretch
1470	C-H in Sp^3 - CH_2	asym. stretch
1270	Si-O in SiOC_3	sym. stretch
1175	C-O in Si-O-C	stretch
1066	Si-O-Si	asym. stretch
840	Si-C in $\text{Si}(\text{CH}_3)_3$	asym. stretch
800	Si-C in $\text{Si}(\text{CH}_3)_2$	asym. stretch

step size ($\approx 0.0001^\circ$). For the XRR measurements we used $\lambda_{\text{k}\alpha}$ – radiation (0.154 nm). The setup can be seen in figure 3.6. For all the measurements a mask of 10 mm and the smallest divergence slit of $\frac{1}{32}^\circ$ was used at the incidence beam side and a 0.1 mm anti scatter slit at the diffracted beam side. The detector was run in receiving slit OD mode. One limitation of this setup is that as a rule of thumb films thicker than ≈ 200 nm can not be measured.

In figure 3.7 we see a measurement of a thin film done by XRR. The film is a copolymer of MAA and HMDSO deposited on native SiO_2 . The two peaks on the left upper side of the plot are the critical angles of the copolymer and the substrate which can be used to calculate the electron density of the film. The most important feature is the occurrence of oscillations in the measurement. These are called Kiessing fringes and occur when the phase difference of the

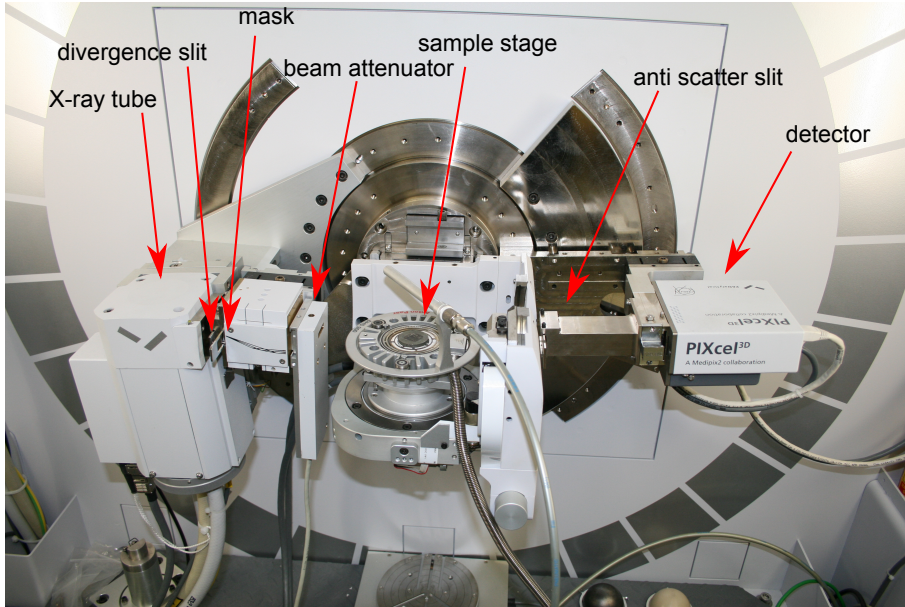


Figure 3.6: Setup for the XRR Measurements on a Panalytical Empyreon.

refracted and reflected beam are a multiple of the wavelength λ . The period of these fringes is inverse proportional to the thickness of the film and can be easily obtained by Fourier analysis of the data.

$$\theta_{m+1} - \theta_m \approx \frac{\lambda}{2t} \quad (3.1)$$

As the period of the fringes gets smaller with increasing thickness the limited resolution of the method explains why there is an upper limit for this technique. It was experimentally determined that the steepness of the slope increases as the film gets rougher. Therefore it is possible to calculate the root mean square roughness of the film by obtaining the slope of the data. [28] To obtain the

3 Experimental

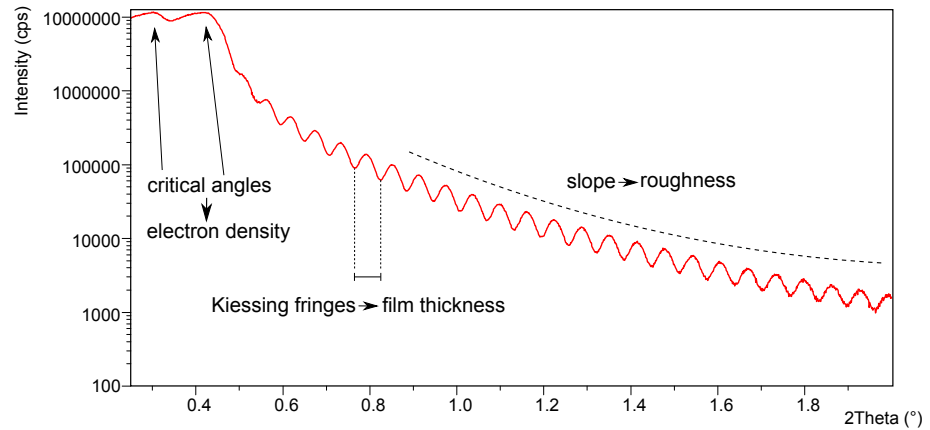


Figure 3.7: Example of a XRR measurement. The period of the Kiessing Fringes which originate from interference effects is inverse proportional to the film thickness. For more detailed explanation see text.

parameters from the measurement the data is fitted with the software X'pert Reflectivity. However as I was mostly interested in the thickness of the film I generally used Fourier analysis to calculate the thickness. The Fourier analysis imposes an error of $\approx 2 - 5 \%$ on the results. However the error of the thickness could be substantially higher since we obtain a height gradient on the sample due to the deposition process.

3.3.3 Profilometry

When the produced films exceeded the 200 nm limit of the XRR method we used profilometry to measure the thickness. The working principle can be seen in figure 3.8. A needle is dragged over the surface and measures the profile of the film. To get the thickness the film over a small area has to be fully removed.

3.3 Film Analysis

This is usually done by making a scratch over the whole length of the sample. Care has to be taken that one removes all of the film but does not remove any substrate. Also the result can be influenced by the hardness of the film and by the speed the needle is dragged. The profilometer used was a Dektak II A.

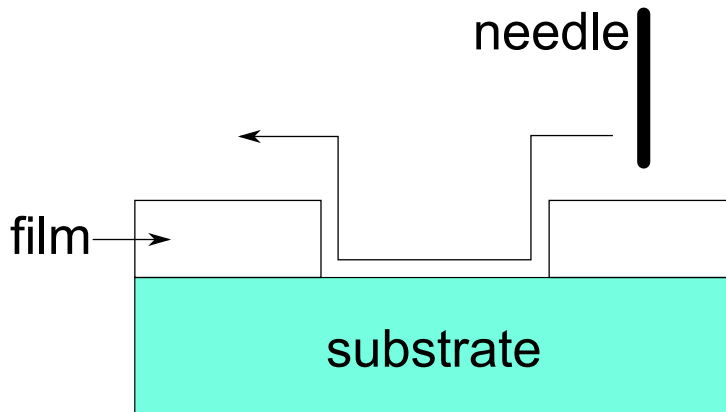


Figure 3.8: Working principle of a profilometer.

3.3.4 Water Contact Angle Measurement

The wettability of a surface is an interesting quantity to investigate. It gives an idea on how the surface interacts when it comes into contact with a liquid. The most important parameter to investigate is the contact angle of the liquid as it sits on the surface. We have a high wettability for contact angles $< 90^\circ$ and a low wettability for angles $> 90^\circ$.

In figure 3.9 we see drops of liquid on a surface that exhibit different contact angles. For angles lower than 90° one can see a wetting behavior of the liquid whereas for angles above 90° the liquid is getting more and more spherical. The aim of achieving a perfect sphere comes from the surface tension of the

3 Experimental

liquid which always tries to minimize the surface free energy which can be achieved by minimizing the surface area. However the surface tension is always competing with other forces (such as gravity), which all together finally give the liquid its shape.

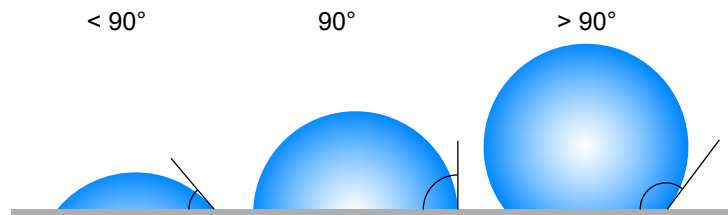


Figure 3.9: Explanation of the water contact angle.

As there are many metastable states a water droplet can get stuck in on a surface it is useful to also investigate the dynamic contact angle (advancing and receding contact angle). The method is shown in figure 3.10. In the advancing regime the angle (θ_a) increases as the volume of the drop gets bigger. The angle just before the contact line moves is the advancing angle. In the receding method the volume of the drop is decreases and the shape flattens out until the contact line slides back (receding angle θ_r) to create a more spherical shape again.

The hysteresis between the advancing and receding angle is generally explained due to roughness or heterogeneity. As a surface gets rougher the hysteresis increases as the microscopical changes in height act as barriers. If the produced films are not homogeneous it could be hydrophobic domains that can also act as barriers. [29] One other important property which can lead to an increase of the hysteresis is the change in the chemical composition due to the surface being exposed to the liquid. For example if you have flexible chains made of hydrophobic and hydrophilic parts they can rearrange so that in the

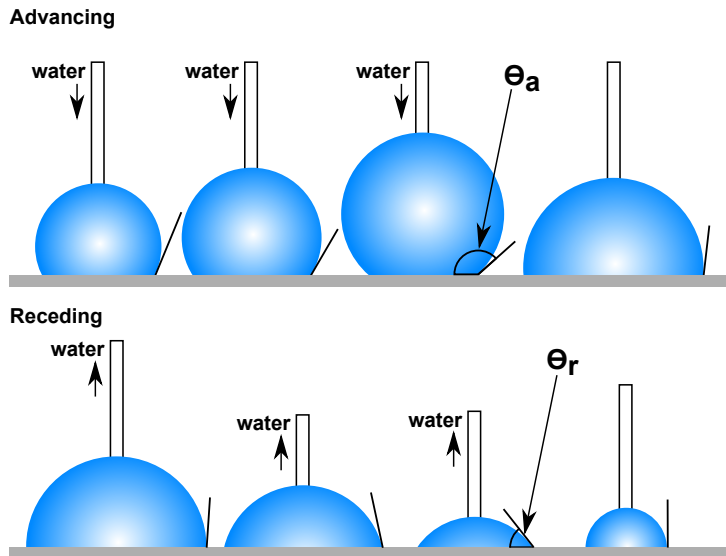


Figure 3.10: Advancing and receding water contact angle measurement

wetted region the hydrophilic groups orient towards the water which changes the wettability of the surface hence a bigger hysteresis. [30]

3.3.5 Electrochemical Impedance Spectroscopy (EIS)

EIS is a method to study the dielectrical response of materials due to an applied AC field as a function of frequency. From the dielectrical function of a material one can calculate the impedance. Due to its applicability and the possibility to measure the membranes conductivity in situ during fuel cell operation the method has been widely used for PEM fuel cell testing and diagnosis. [3]

In figure 3.11 we see the setup for the measurement. In solution it is important to consider that charge transport can occur not only through the membrane

3 Experimental

but also through the liquid. When the imaginary part of the impedance is zero the resistance can be calculated by

$$\frac{1}{R_{\text{total}}} = \frac{1}{R_{\text{membrane}}} + \frac{1}{R_{\text{solution}}} \quad (3.2)$$

Therefor to get a reliable measurement the resistance of the solution must be significantly greater than the resistance of the membrane $R_{\text{solution}} \gg R_{\text{membrane}}$. [31]

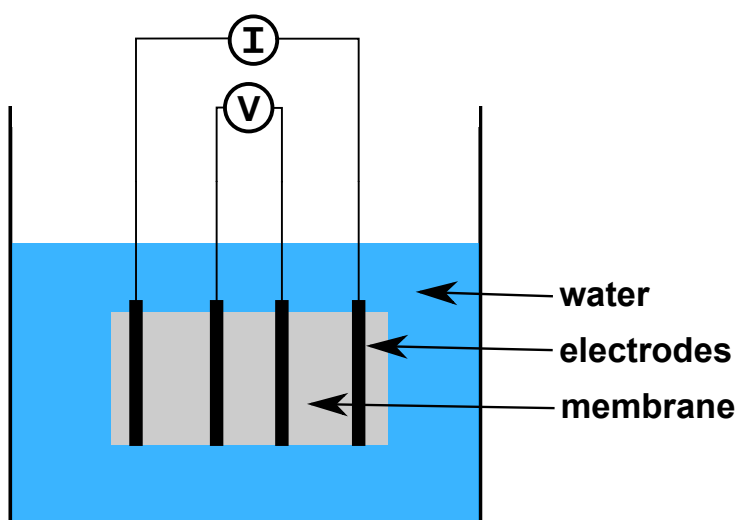


Figure 3.11: Setup for the EIS measurements. The membrane is connected to a 4-point-probe measurement setup and immersed in water.

The device used for EIS was a Gamry Instruments, Reference 600. The membranes were measured in a frequency range from 0.1 – 10000 Hz with a root mean square voltage of 50 mV. The membranes were deposited on polyethylene terephthalate (PET) substrates with a length and width of 2.5 cm and 1.3 – 1.6 cm, respectively. Measurements were carried out in \approx 400 ml high

purity water with a resistance of $17.4\text{ M}\Omega$ with a 4-point-probe technique. The resistance of the solution (R_{solution}) was measured immediately after every membrane was measured.

3.4 Reactor set-up

In this section I want to write about the experimental problems we ran into as we were setting up the reactor and adjusting it to achieve optimal working conditions. In figure 3.12 one can see the initial setup of the reactor as we started out doing PECVD. Note that the sole difference to the reactor setup now is that we had only one gas inlet from the top instead of another one from the side.

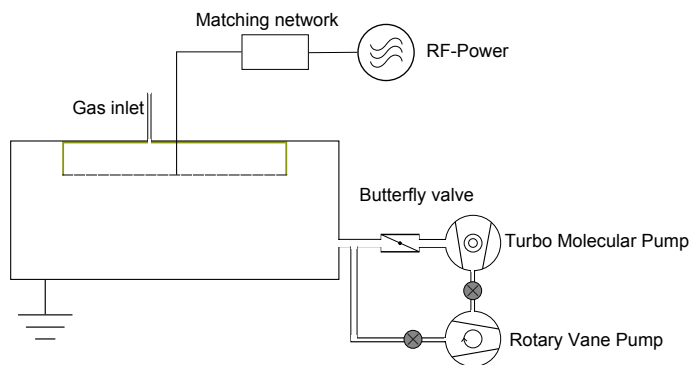


Figure 3.12: Initial reactor setup as we started with PECVD.

The general idea behind this configuration is that using a shower head as we do distributes the gases more homogeneously over a wider area of the reactor. Also flowing all the gases from one side enhances the homogeneity as it provides a mixing of the gases even before they enter the reactor.

3 Experimental

The problem we had with this configuration is that although we were able to deposit HMDSO over a range of parameters we generally failed to deposit MAA. One reason for this can be that we heated the monomer line only until ≈ 5 cm before the reactor chamber (can be seen in figure 3.2). Since the MAA is not very volatile and tends to condensate when it comes into touch with cold surfaces this could mean that we "lose" MAA in the line and also during the calibration of the flow rate on the top electrode. During operation this electrode heats up but the flow rate is determined before power is applied to the electrode and hence it is also still cold. However the condensation on the top electrode should be very small as the flow rates are calibrated at too low pressure for condensation to occur.

Another problem and maybe the biggest one of all was that at the beginning we used a Pfeiffer Vacuum Compact Full Range Gauge PKR 251 to measure the pressure. Unfortunately this type of pressure sensor is gas-sensitive and hence showed wrong results in our case. Therefore in all the depositions prior to the introduction of the new gas independent pressure sensor we can not be certain about the flow rate of the monomers we flew. This seems to be especially true for MAA as the pressure gauge seemed to have even more problems with this monomer.

The next problem was that after ≈ 20 depositions it was observed that there were jumps in the flow rate of MAA. After the system was evacuated for a longer period (one night or one weekend) the flow rate was fine at the beginning but after a few depositions it started to decrease. The problem was solved by heating the needle valve to 100°C , opening it completely and leaving the system to evacuate over the weekend. The problem might have been that the needle valve was heated not thoroughly enough and therefore was probably starting to get clogged with the condensed monomer. For the system to work

3.4 Reactor set-up

properly it is essential that the monomer lines are heated everywhere to the required temperature and that especially critical spots do not drop below this temperature.

Finally another problem was due to a leak in the butterfly valve. However the leak was not permanent. At any static position the valve sealed but once it moved over a certain position it started to leak. The leak was in the drive shaft of the valve. The reason for this leak was maybe due to powder that was formed during the plasma deposition and covered the valve and the o-ring. After many opening and closing cycles a small leak formed. We improved the system by installing a fine mesh of stainless steel between the reactor and the valve that holds back a substantial amount of powder.

4 Results and Discussion

In this chapter the results of the measurements that were obtained by the methods explained in the previous chapter will be discussed. The films were produced from pure HMDSO, pure MAA and HMDSO plus MAA combined.

4.1 Homopolymers

As we started we were at first interested on how the monomers separately behave in the reactor. Therefore a test series in which only one species of monomers mixed with argon was used to produce the thin films.

4.1.1 Pure Hexamethyldisiloxane (HMDSO)

In table 4.1 one can see the flow rate and the deposition rate of the series. All films were deposited at a pressure of $p_{\text{work}} = 500 \text{ mTorr}$ and at a power of 25 W. The flow rate of argon was adjusted such that the total flow rate equals approximately 12 sccm. The plot of the data can be seen in figure 4.1.

4 Results and Discussion

Table 4.1: Experimental data for the deposition of the films from HMDSO. The data is plotted in figure 4.1. The thickness measurements were performed by XRR. R_{dep} is the deposition rate.

Sample Number	81	82	83	84	85
Flow rate HMDSO / sccm	0.5	0.9	1.30	1.7	2.4
Flow rate Argon / sccm	11.5	11	10.5	10	9.3
$R_{\text{dep}} / \frac{\text{nm}}{\text{min}}$	4.5	6	7.1	6.3	6.8
$\Delta R_{\text{dep}} / \frac{\text{nm}}{\text{min}}$	0.1	0.3	0.1	0.1	0.1

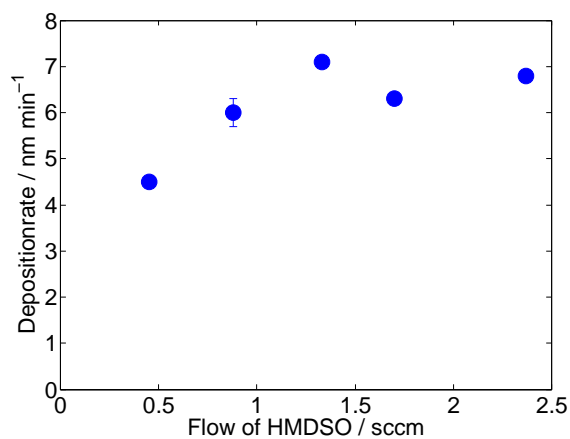


Figure 4.1: Plot of the deposition rate as a function of an increasing flow rate of HMDSO. The deposition rate increases because the ratio of HMDSO to argon increases. The numerical values of the data and errors can be seen in table 4.1.

The deposition rate increases slowly from $4 \frac{\text{nm}}{\text{min}}$ to $7 \frac{\text{nm}}{\text{min}}$ as we increase the monomer flow rate. This behavior was expected since the ratio of HMDSO to argon gets bigger. This means that there is more material to deposit in the

reactor and therefore the deposition rate increases.

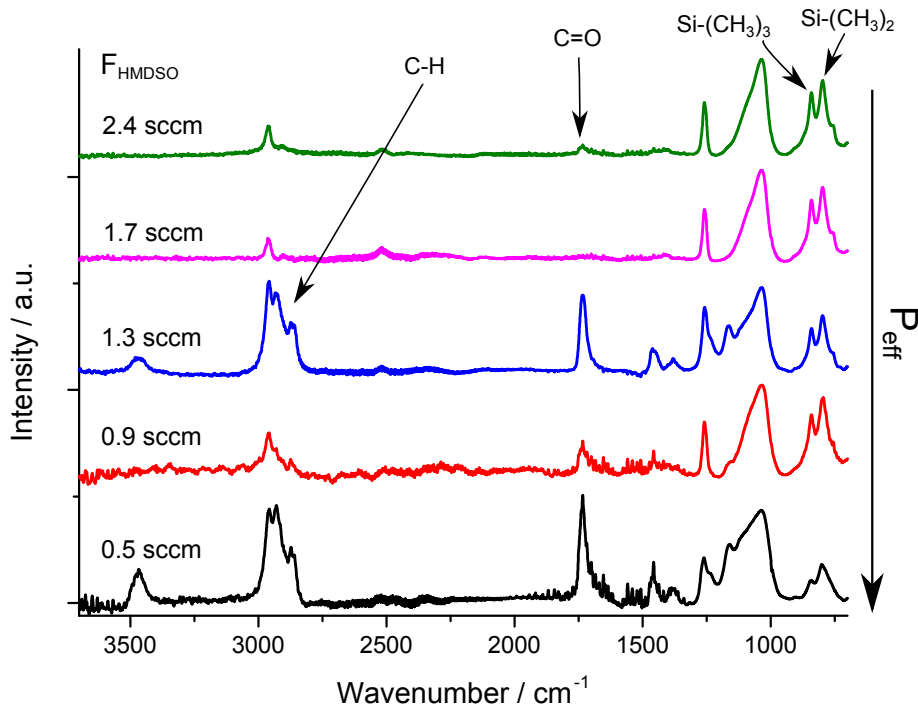


Figure 4.2: FTIR-spectra for increasing flow rate of HMDSO. In Dep. 81-83 MAA from the reactor walls desorbes and is incorporated which leads to the strong C-H and C=O peak. No strong changes in the HMDSO Peaks are observed.

In figure 4.2 one can see the FTIR-spectra of the series. The right vertical axis of the plot shows the behavior of the Yasuda factor. When the flow rate decreases the effective power increases (see section 2.3.2). The reactor was apparently contaminated with MAA and therefore we see in the first three depositions the strong C=O peak at 1700 cm^{-1} and an additionally strong signal of the C-H bond at 2900 cm^{-1} . One explanation of these strong signals could be that although

4 Results and Discussion

HMDSO has more CH_3 groups in its structure the groups in the MAA have a bigger dipole moment. As explained in section 3.3.1 the intensity depends on the quantity of material and on the dipole moment. This could mean that MAA deposited on the substrate in the form of unreacted monomer. After that either the reactor got coated with HMDSO or the contamination evaporated during the three depositions and hence the peaks disappear. The contribution of the HMDSO does not vary dramatically. As the effective power decreases we see that the $\text{Si}-(\text{CH}_3)_3$ peak increases slightly compared to the $\text{Si}-(\text{CH}_3)_2$ peak adjacent to it. This means that as the effective power is reduced less Si-C bonds are broken and therefore slightly more $\text{Si}-(\text{CH}_3)_3$ groups are incorporated into the polymer.

4.1.2 Pure Methacrylic Acid (MAA)

Table 4.2 shows the the flow rates and the deposition rates for this series. The films were deposited at a pressure of 500 mTorr and a power of 25 W. The flow rate of argon was adjusted such that the total flow rate equals approximately 12 sccm. The plotted data can be seen in figure 4.3.

For the MAA we observe a very different behavior than for the HMDSO. As we increase the flow rate we also as expected see an increase in the deposition rate. However the deposition rate is almost 4 times as large as for the HMDSO. This might be due to the setup of the reactor. One possibility could be that the MAA is more reactive due to the weak pi bond of the C=C group and therefore one achieves a higher deposition rate.

Another but not so likely explanation could be that the HMDSO travels through the shower head configuration before it arrives in the reactor whereas the MAA flowing in from the side probably has some sort of preferred direction.

4.1 Homopolymers

Table 4.2: Experimental data for the deposition of the films from MAA. The data is plotted in figure 4.3. The thickness measurements were performed by XRR. R_{dep} is the deposition rate.

Sample Number	90	91	92	93	94
Flow rate MAA / sccm	0.5	1	1.5	2	2.5
Flow rate Argon / sccm	11.5	11	10.5	10	9.5
$\Delta R_{\text{dep}} / \frac{\text{nm}}{\text{min}}$	1.7	3.7	7.5	11.3	22.6
$\Delta R_{\text{dep}} / \frac{\text{nm}}{\text{min}}$	0.1	0.1	0.1	0.3	0.5

Increasing the flow of HMDSO therefore does not influence the deposition rate as drastically as increasing the MAA flow rate.

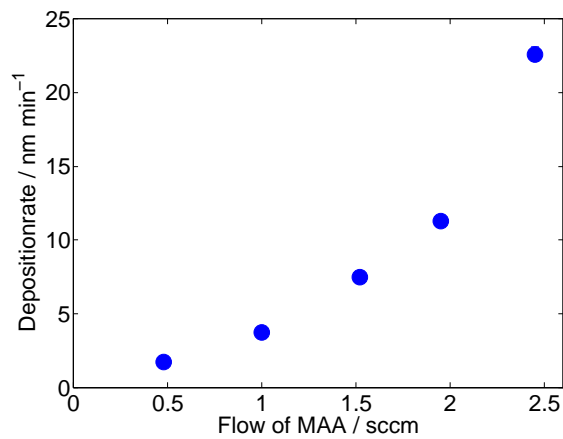


Figure 4.3: Deposition rate as a function of the MAA flow rate for pure MAA homopolymers. The deposition rate shows a strong increase with the MAA flow rate. The numerical values of the data and errors can be seen in table 4.2.

4 Results and Discussion

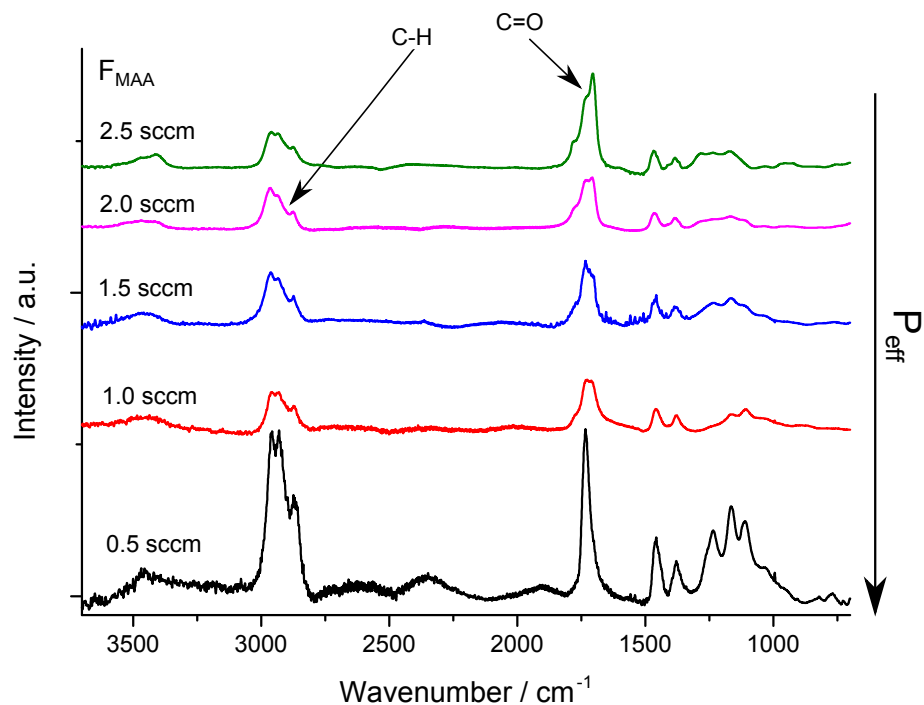


Figure 4.4: FTIR-Spectra for increasing flow rate of MAA. One can see that the position of the C=O peak shifts.

The FTIR-spectra of the series can be seen in figure 4.4. The high intensity at 0.5 sccm can not be fully trusted as the film was only 50 nm thick. However an interesting conclusion can be drawn from the peak positions. When we zoom into the region around the C=O peak (figure 4.5) one can see that this peak consists of two to three individual components. From the structure of our monomers we would expect to have only one contribution to the C=O absorption, coming from the COOH group (1705 cm^{-1}). However already at low effective power (2.5 sccm) it can be seen that a COOR component (1735 cm^{-1})

4.1 Homopolymers

is present. This is due to the fragmentation and recombination of the COOH with other radicals of the plasma phase as represented in fig 4.6.

At high powers we break most of the O-H bonds. Subsequently the remaining COO reacts some other group to form COOR (ester). As we go to lower power we retain more of the original COOH groups and therefore the C=O peak at 1705 cm^{-1} increases.

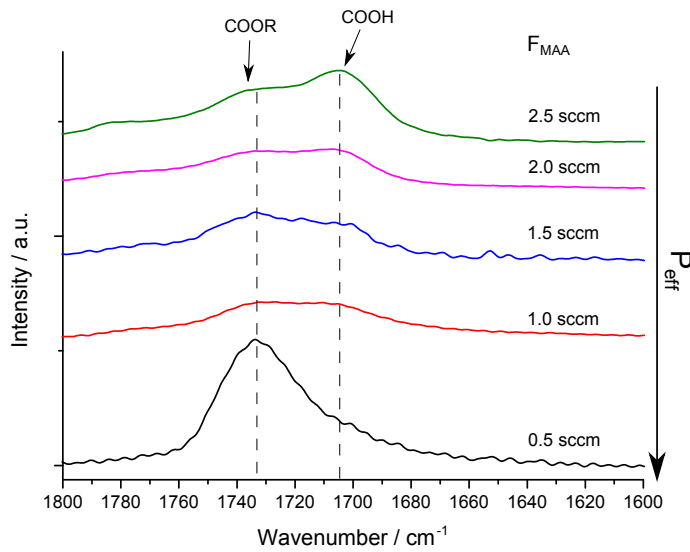


Figure 4.5: FTIR-Spectra zoomed to the C=O oscillation peak.

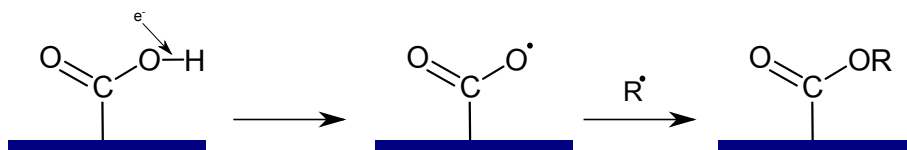


Figure 4.6: COOR creation process. At higher powers it gets more likely to break the O-H bond. A radical can then combine with the group to create COOR.

4.2 Copolymers

4.2.1 Copolymer of constant HMDSO and varying MAA

The next step was to combine the two monomers and look at the outcome as different parameters are varied. This series was deposited at 25 W and 500 mTorr. The argon flow rate was varied so that the resulting total flow rate equals approximately 12 sccm. Deposition rate and flow rates can be seen in table 4.3.

Table 4.3: Deposition rate and flow rates for the deposition series. The thicknesses were measured with XRR (Samples 103 and 104) and profilometry (Samples 100-102). R_{dep} is the deposition rate.

Sample Number	100	101	102	103	104
Flow rate MAA / sccm	0.6	1	1.5	2	2.3
Flow rate Argon / sccm	9.5	9	8.5	8	7.7
$R_{\text{dep}} / \frac{\text{nm}}{\text{min}}$	38	76	170	169	163
$\Delta R_{\text{dep}} / \frac{\text{nm}}{\text{min}}$	1.3	1.9	1.8	7.0	6.9

In figure 4.7 one can see the deposition rate as a function of the MAA flow rate. One can see that in comparison with the flow rates of the depositions with only one species of monomer we get to a much higher deposition rate when we combine the monomers. This might be caused on the one hand by an increased chemical reactivity of the gas mixture when both monomers are combined or on the other hand by the increased monomer to argon ratio.

In the FTIR spectra seen in figure 4.8 one can see changes in the chemical composition. Careful inspection of the Si-C oscillations show first of all an

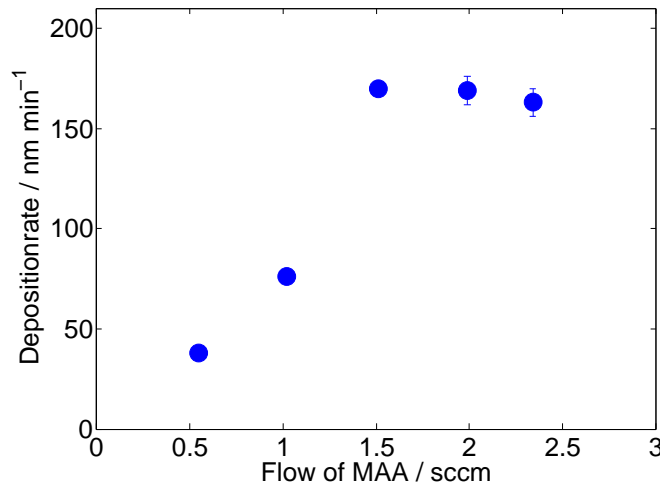


Figure 4.7: Deposition rate as a function of the MAA flow rate. The numerical values of the data and errors can be seen in table 4.3.

overall decrease in intensity as the effective power is lowered. Secondly one can see that the intensity of the Si-(CH₃)₃ and Si-(CH₃)₂ double peak shifts. One possible explanation for this can be that as we go to lower powers we break less of the Si-C bonds retaining more Si-(CH₃)₃ groups of the original HMDSO structure. Therefore as the HMDSO is a very volatile molecule simply more of the molecules get pumped off and less is deposited and incorporated in the copolymer which explains the decrease in intensity.

4 Results and Discussion

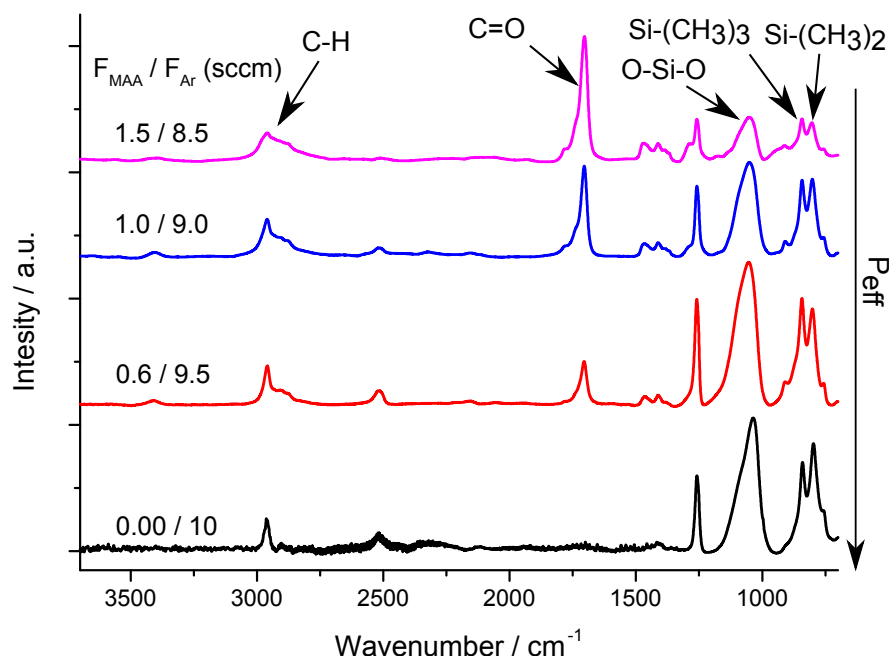


Figure 4.8: FTIR-spectra of a series with varying MAA flow rate. One can see a clear increase in the MAA content of the copolymer whereas the HMDSO decreases.

4.2.2 Copolymer of constant MAA and varying HMDSO

In this series the flow rate of MAA was kept constant at 2 sccm and the HMDSO flow rate was varied. The films were deposited at a pressure of 500 mTorr and a power of 25 W. The flow rate of argon was adjusted so that the resulting total flow rate equals approximately 12 sccm. The parameters of the deposition can be seen in table 4.4.

By combining the two monomers we can arrive at a much higher deposi-

Table 4.4: Deposition parameters and deposition rate for constant MAA and varying HMDSO. The data is plotted in figure 4.9. The thicknesses were measured with profilometry. R_{dep} is the deposition rate.

Sample Number	95	96	97	98	99
Flow rate HMDSO / sccm	0.5	1	1.5	2	2.5
Flow rate Argon / sccm	9.5	9	8.5	8	7.5
$R_{\text{dep}} / \frac{\text{nm}}{\text{min}}$	32	50	108	157	202
$\Delta R_{\text{dep}} / \frac{\text{nm}}{\text{min}}$	0.5	0.5	5.3	7.0	4.6

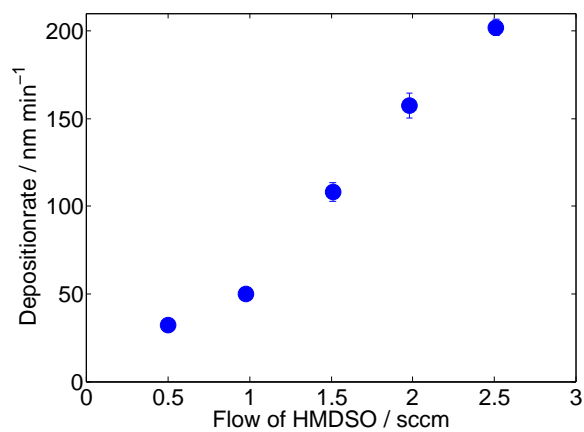


Figure 4.9: Deposition rate as a function of the HMDSO flow rate with a constant flow rate of MAA. High deposition rate can be achieved compared to depositing pure monomers. The numerical values of the data and errors can be seen in table 4.4.

tion rate than depositing just one of them (figure 4.9) which can be seen by comparing deposition rates at similar flow rates. The reason for this could as

4 Results and Discussion

previously stated be the increasing monomer to argon ratio. However another possibility could be that the addition of MAA enhances the deposition rate because of the weak π bond of the $C=C$ group. This π bond is easily broken therefor increasing the reactivity which might increase the deposition rate. Also the further decrease in power leads to an increase in the deposition rate which is explained in section 2.3.2.

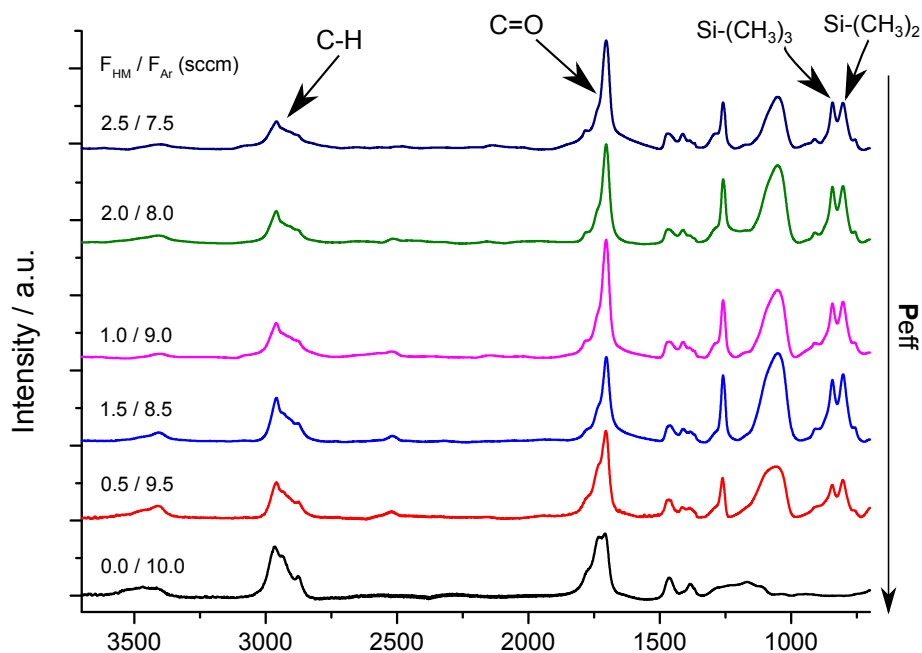


Figure 4.10: FTIR-Spectra for an increasing HMDSO flow with a constant flow rate of MAA. One can see the shift of the $C=O$ peak and the switch of the $Si-(CH_3)_3/Si-(CH_3)_2$ double peak in intensity.

In the FTIR-Spectra in figure 4.10 two effects can be seen. First one sees that as with the depositions of pure MAA the intensity of the $C=O$ components shifts

with lower effective powers towards the COOH peak at 1705 cm^{-1} instead of the previously discussed COOR peak 1735 cm^{-1} . Also we see again the shift in intensity of the double peak in the HMDSO spectrum around 800 cm^{-1} .

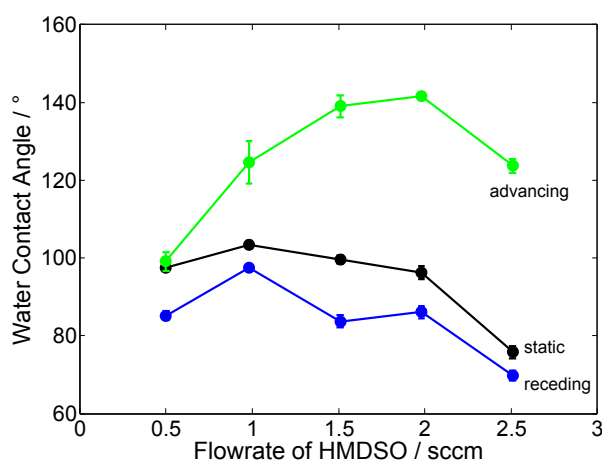


Figure 4.11: Water contact angle measurement for an increasing HMDSO flow rate. One observes an increase in the hysteresis as the flow of HMDSO increases.

In figure 4.11 one can see the results of the water contact angle measurements. The hysteresis of the advancing and receding contact angle increases as we increase the HMDSO flow rate. As plasma deposition processes generally produce homogeneous films with a very low roughness we attribute the hysteresis of these films to changes in chemical structure as the films surface comes into contact with the water. One reason for this could be that the flexibility of the polymer chains in the amorphous structure gets bigger as we increase the HMDSO flow rate.

4 Results and Discussion

4.2.3 Variation of the total flow rate with a constant ratio

The films were deposited at 500 mTorr and 25 W. The total flow rate is varied while the ratio between the two monomers and the argon is kept constant. The ratio was chosen to be a 1:2:9 ratio of HMDSO, MAA and argon, respectively.

This has the advantage that one can really investigate how the Yasuda factor influences the chemical structure of the film. If the effective power was not influenced by the flow rates and the ratio between the species is kept constant the chemical composition of the film should not vary at all as the flow rates are increased and only the deposition rate should increase since we are increasing the amount of material in the reactor. However in these results one can see this is not the case and that the flow rates do have an influence on the chemical composition. Therefore the Yasuda factor is applicable for our system and one can try to explain some of the effects with it. Additionally in the previous depositions we increased one monomer while keeping the other constant which changes not only the flow rate but also the ratio between the flowing species. This is not optimal for investigating the alterations caused predominantly by the Yasuda factor.

Figure 4.12 shows the deposition rate of the series. It increases almost linearly as the flow rates are increased. This is probably simply because there is more material in the reactor to deposit. The deposition parameters and the deposition rate can be seen in table 4.5

From the FTIR-Spectra in figure 4.13 interesting changes can be observed. First one can see from the highest to the lowest power how the HMDSO Si-(CH₃)₃/Si-(CH₃)₂ double peak gradually switches the intensity. Secondly one can observe that as we go to lower powers more and more of the COOH groups of the MAA are preserved and incorporated in the structure. If the assumption of

Table 4.5: Deposition parameters and deposition rate. The ratio between the species is kept constant while the total flow rate changes. The thicknesses have been measured by XRR. R_{dep} is the deposition rate.

Sample Number	105	106	107	108	109	110
Flow rate HMDSO / sccm	0.5	0.6	0.7	0.8	0.9	1
Flow rate MAA / sccm	1	1.2	1.4	1.6	1.8	2
Flow rate Argon / sccm	4.5	5.4	6.3	7.2	8.1	9
Total flow rate / sccm	6	7.2	8.4	9.6	10.8	12
$R_{\text{dep}} / \frac{\text{nm}}{\text{min}}$	16	22	28	35	42	49
$\Delta R_{\text{dep}} / \frac{\text{nm}}{\text{min}}$	0.6	0.4	0.5	0.9	0.6	1.3

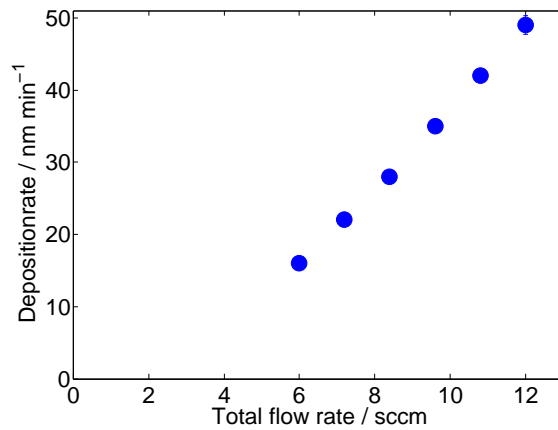


Figure 4.12: Deposition rate in dependence of a changing total flow rate with a constant ratio of species. The numerical values of the data and errors can be seen in table 4.5.

4 Results and Discussion

section 4.1.1 that the signal from the unreacted MAA monomer is a lot stronger is correct we can assume from the less intense signal of the C-H group that although we retain most of the COOH groups the molecule is still broken and chemically bound in the structure.

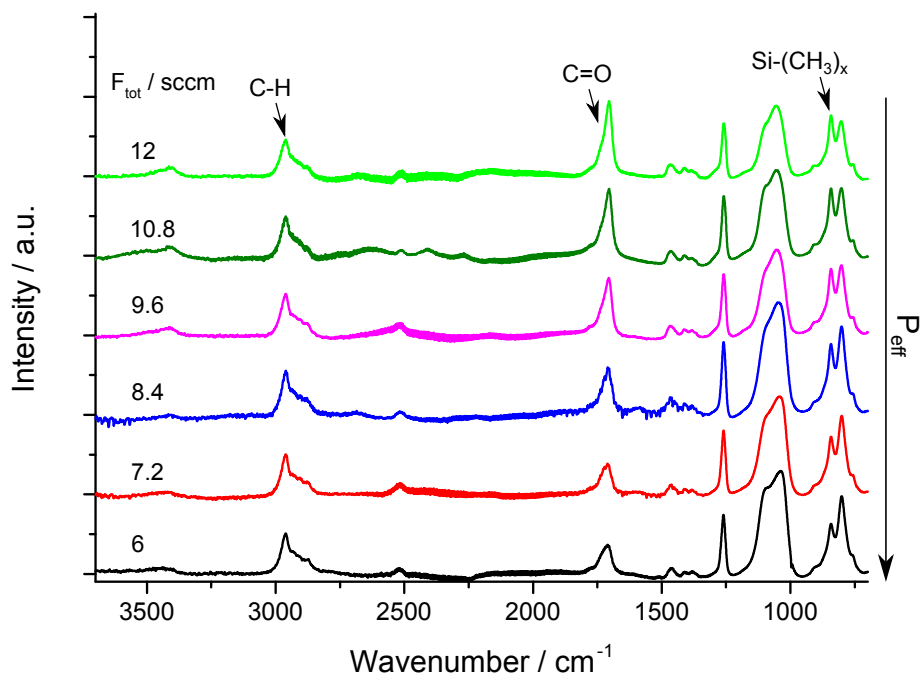


Figure 4.13: FTIR-Spectra for a changing total flow rate with a constant ratio of species. The x can stand for 3 or 2 corresponding to absorptions at 840 cm⁻¹ and 800 cm⁻¹, respectively.

4.2.4 Variation of argon flow rate at a constant flow of monomers

In the paper of Hegemann et al. it is shown that the introduction of inert gases has no influence on the chemical composition of the film. [22] We wanted to investigate if this is also the case with our monomers and our reactor. Therefore a series with varying argon flow rate was deposited. The films were produced with flow rates of $F_{\text{HMDSO}} = 1 \text{ sccm}$ and $F_{\text{MAA}} = 1 \text{ sccm}$ at a pressure of 500 mTorr and a power of 25 W.

The deposition parameters can be seen in table 4.6. The data has been plotted in figure 4.14. For an increasing flow rate of argon the deposition rate steadily decreases which might be caused by two effects. On the one hand it could be as previously discussed the effect of diluting the monomer. On the other hand it could be that increasing the argon also generates more electrons (more collisions) which could cause a higher fragmentation. Smaller fragments are more likely to react in the gas phase. When this happens we observe powder formation and lower deposition rates.

Table 4.6: Deposition parameters for a series with a variation in the argon flow. The thicknesses were measured by XRR. R_{dep} is the deposition rate.

Sample Number	130	131	132	133	134
Flow rate Argon / sccm	4	8	12	16	20
$R_{\text{dep}} / \frac{\text{nm}}{\text{min}}$	46	40	31	27	24
$\Delta R_{\text{dep}} / \frac{\text{nm}}{\text{min}}$	1.3	1.3	0.7	0.9	0.6

The FTIR Spectra are seen in figure 4.15. The data of the 4 sccm and 12 sccm film showed strong noise at the position where the C=O peak is. Therefore these

4 Results and Discussion

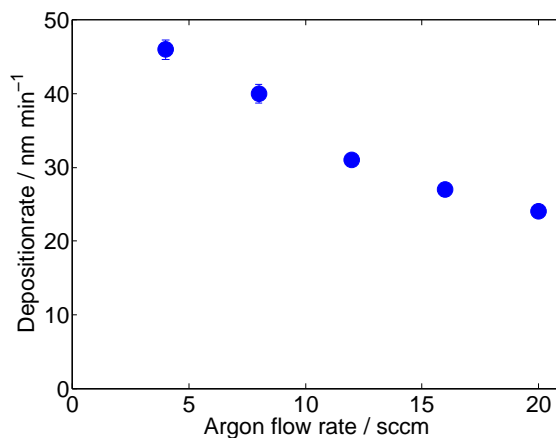


Figure 4.14: Deposition rate for a varying argon flow rate. The numerical values of the data and errors can be seen in table 4.6.

two measurements have to be considered with caution. Anyhow the changes in the chemical composition are relatively small. The HMDSO double peak around 800 cm^{-1} only changes by a tiny amount except from the deposition with 4 sccm to 8 sccm. The C=O peak increases in intensity however it is also relatively broad in comparison with previous depositions. As mentioned in section 4.2.6 it has been shown in literature that argon has no influence in the chemical composition however some papers show it has an influence on the deposition rate [22]. We find similar results in this series. The chemical composition shows only limited changes and the deposition rate decreases.

4.2 Copolymers

Table 4.7: Thickness measurements before and after immersion in water for 30 min. The errors of the measurements were estimated to be $\approx 3\%$.

Sample Number	Argon Flow / sccm	d_{before} / nm	d_{after} / nm
130	4	182	151
131	8	161	131
132	12	172	152
133	16	155	143
134	20	157	144

Water stability tests showed that the samples were stable after being immersed in water at room temperature for 10 min. The thickness of the samples has been remeasured after 10 weeks on air and 20 min in water. Table 4.7 shows the comparison between the initial thickness and the thickness after a total of 30 min in water. All of the samples show a decrease in thickness after 30 min which means that they dissolve.

4 Results and Discussion

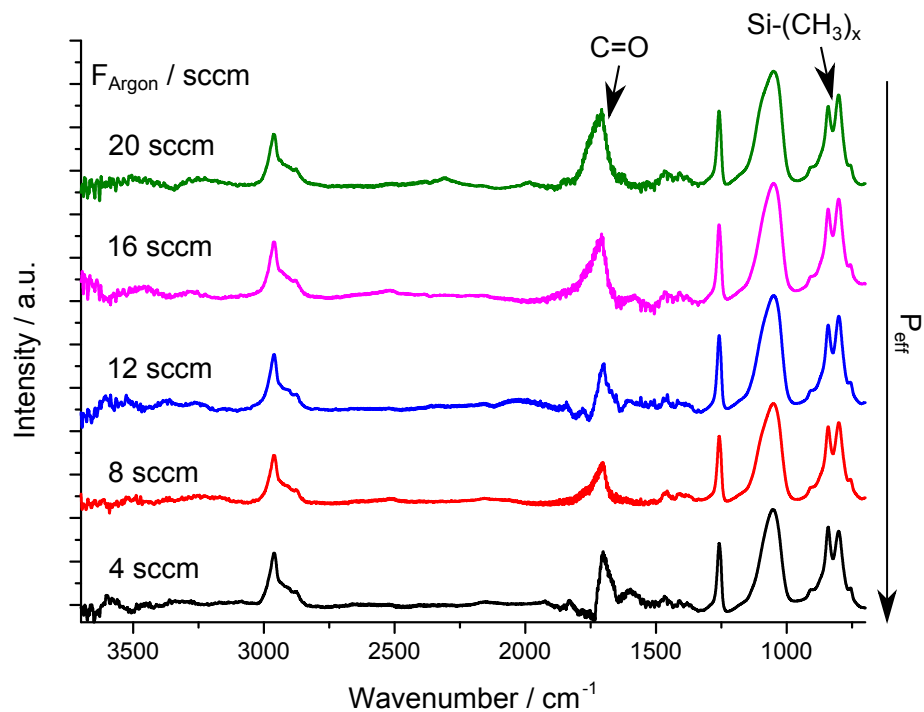


Figure 4.15: FTIR-spectra for a varying argon flow rate. The x can stand for 3 or 2 corresponding to absorptions at 840 cm^{-1} and 800 cm^{-1} , respectively.

4.2.5 Variation of power at a constant flow of monomers and argon

If the Yasuda parameter is really applicable for this system similar results to section 4.2.3 (change of total flow rate while ratio and applied power stay constant) should be obtained if the flow rate is kept constant while the applied power is varied. The series has been deposited with a flow of MAA and HMDSO of 1 sccm and a flow of 4 sccm of argon. The films were deposited at 500 mTorr.

In table 4.8 one can see the applied power and the deposition rate. The plotted data can be seen in figure 4.16.

Table 4.8: Applied power and deposition rate. The thicknesses have been measured by XRR. R_{dep} is the deposition rate.

Sample Number	135	136	137	138	139
Power / W	20	25	30	40	50
$R_{\text{dep}} / \frac{\text{nm}}{\text{min}}$	56	46	42	39	32
$\Delta R_{\text{dep}} / \frac{\text{nm}}{\text{min}}$	1.5	1.5	1.3	0.8	1.0

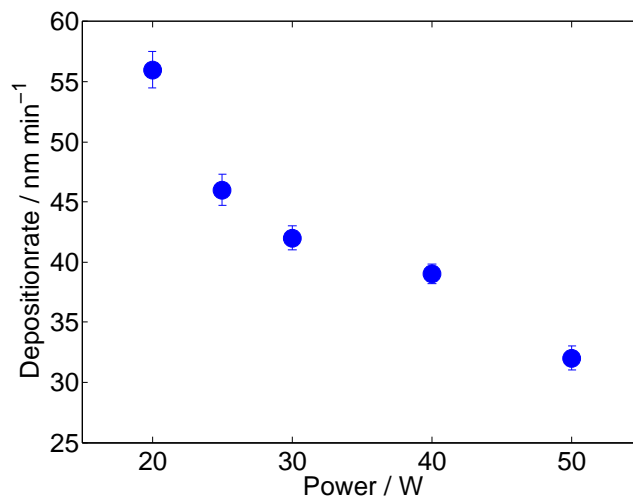


Figure 4.16: Deposition rate as a function of power. The numerical values of the data and errors can be seen in table 4.8.

For an increasing power the deposition rate decreases. This makes sense

4 Results and Discussion

since at high powers more bonds are broken and therefore one ends up with smaller fragments decreasing the deposition rate. Another possibility could be that since at higher powers the ion bombardment of the film increases which could induce the cleavage of some groups that are already forming on the film. However at low powers we retain most of the molecules which leads to the formation bigger blocks that increase the deposition rate.

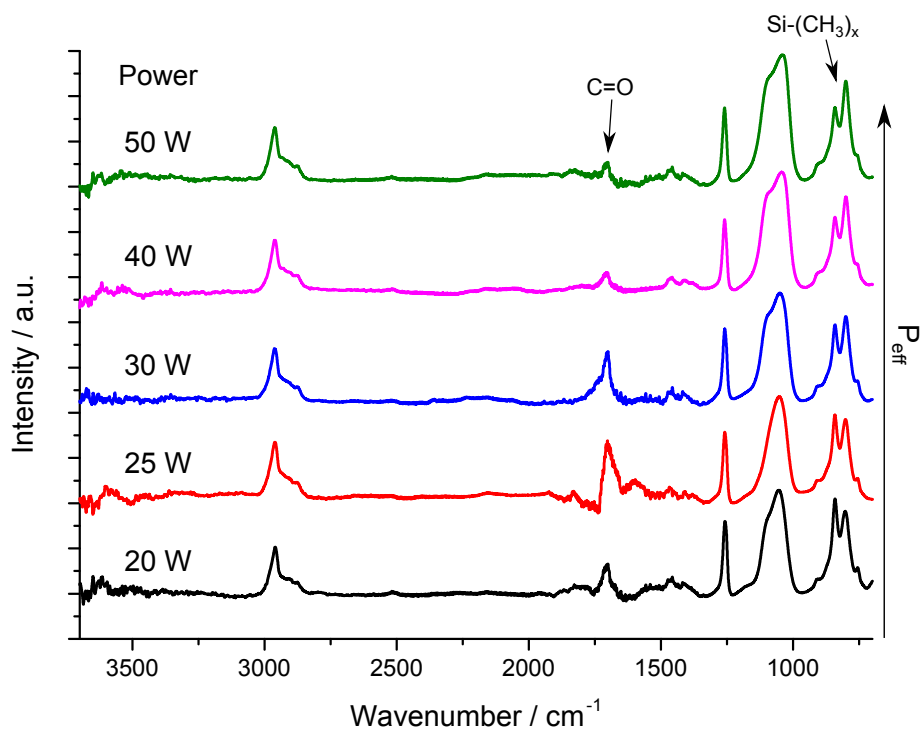


Figure 4.17: FTIR-spectra for varying applied power. The x can stand for 3 or 2 corresponding to absorptions at 840 cm^{-1} and 800 cm^{-1} , respectively.

As we look at the FTIR-spectra in figure 4.17 one can observe the exact

same behavior as for previous depositions. As the effective power increases the Si-(CH₃)₃ / Si-(CH₃)₂ double peak shifts in intensity towards the Si-(CH₃)₂ peak. The analysis for the C=O peak was tricky but one can see that the C=O decreases as the power increases and that it drops significantly as we go from 30 W to 40 W. One explanation for this could be that at a certain applied power we supply enough energy to break most of the C=O bonds and therefore this peak vanishes almost completely.

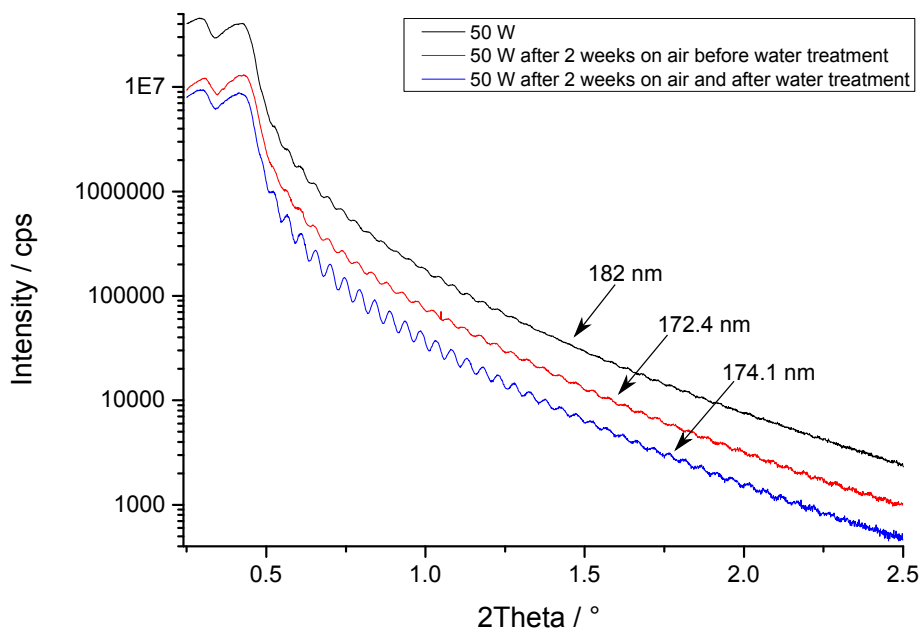


Figure 4.18: XRR stability measurement for the sample deposited at 50 W.

After immersion in water for 10 min at room temperature, the samples deposited at higher power were the ones that after pulling them out of water were immediately dry, due to a higher hydrophobicity. The increasing hydrophobicity

4 Results and Discussion

of the samples can also be seen in the FTIR spectra. As the effective power increases we incorporate more of the HMDSO groups and less of the MAA groups. Swellability measurements performed with the XRR showed a miniscule swelling for the most hydrophobic deposition corresponding to 50 W. Unfortunately the swelling is so small that it falls within the error margin of this method which makes it hard to say if we observe swelling. The XRR measurement can be seen in figure 4.18. The swelling for other depositions can be seen in table 4.9. The samples seem to be unstable at air and even less stable after immersed in water. It can be seen though that increasing the power also increases the stability of the films.

Table 4.9: Thicknesses of the depositions. The first thickness d was measured a few hours after they were deposited. Then the thickness was remeasured after two weeks on air before and after being immersed in water for 20 min. The errors were obtained from the Fourier analysis of the XRR data.

Sample number	Power / W	d / nm	d_{before} / nm	d_{after} / nm
136	20	155 ± 4	128 ± 6	112 ± 6
137	30	180 ± 4	150 ± 5	147 ± 3
139	50	182 ± 6	172 ± 3	174 ± 4

4.2.6 Variation of pressure at constant flow rates

Pressure is the only parameter which does not influence the Yasuda factor directly. However it influences the system in other ways. The series was deposited at a power of 25 W with flow rates of MAA and HMDSO of 1 sccm and 4 sccm for argon. The pressure and the deposition rate can be seen in table 4.10 and

has been plotted in figure 4.19.

Table 4.10: Pressure and deposition rate. The thicknesses were measured by XRR. R_{dep} is the deposition rate.

Sample Number	140	141	130	142	143
Pressure / mTorr	300	400	500	600	700
$R_{\text{dep}} / \frac{\text{nm}}{\text{min}}$	17	30	46	62	110
$\Delta R_{\text{dep}} / \frac{\text{nm}}{\text{min}}$	0.2	0.6	1.3	1.5	2.4

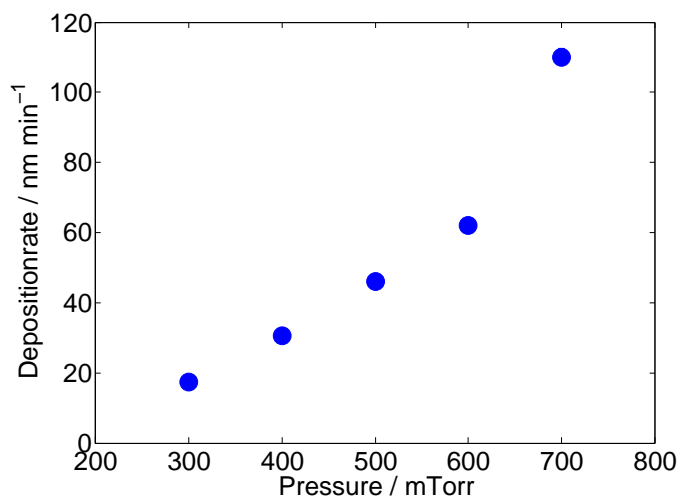


Figure 4.19: Deposition rate as a function of pressure. The numerical values of the data and errors can be seen in table 4.10.

One can see in figure 4.19 that the deposition rate increases dramatically as the pressure is increased. One reason for this could be that as the pressure in the chamber increases the density of particles also increases. This means that

4 Results and Discussion

at higher pressures we have more molecules in the reactor. As there is more material in the chamber more material will deposit on the sample increasing the deposition rate. Secondly having more molecules means that the applied effective power will decrease because the applied power has to be distributed over more molecules. A lower effective power leads to oligomerization and subsequently to a higher deposition rate.

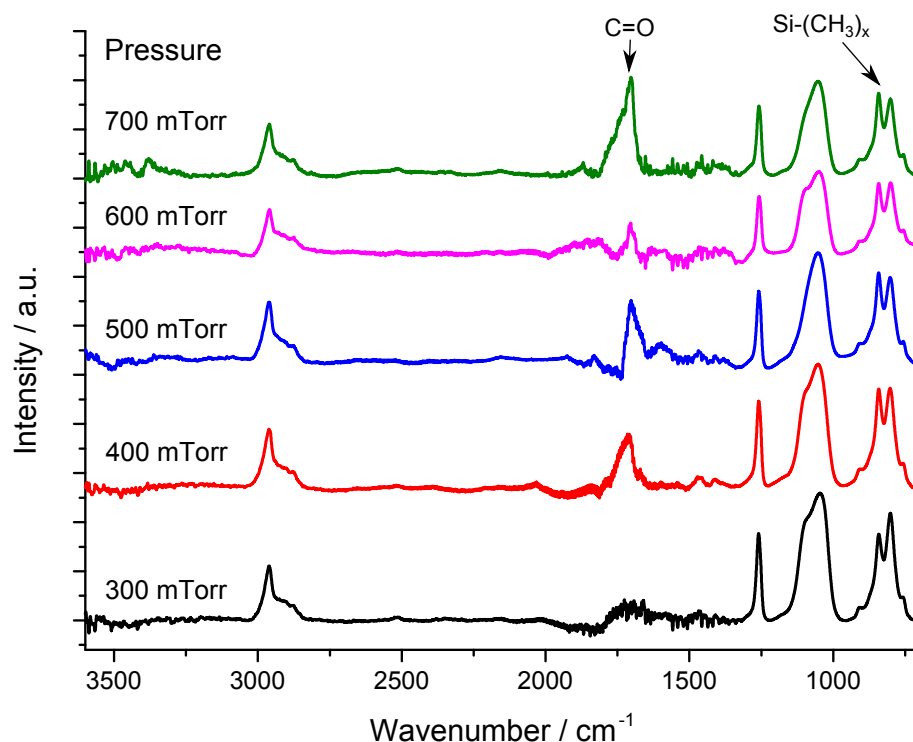


Figure 4.20: FTIR-spectra for varying pressure. The x can stand for 3 or 2 corresponding to absorptions at 840 cm⁻¹ and 800 cm⁻¹, respectively.

As the pressure increases the chemical composition changes as well. As seen

4.2 Copolymers

in figure 4.20 more HMDSO is incorporated at lower pressures because more CH_3 groups are broken. However it seems that for the same reason the MAA decreases for lower pressures. There is one more important quantity which is influence by the pressure namely the ion bombardment. For lower pressures the ion bombardment is higher which should lead to a more stable structure and a greater water stability.

Figure 4.21 shows the water stability of the deposited films after being exposed to water for 1 hour at 20°C . At lower pressures the films are more stable. The reason for this is probably the combination of the higher ion bombardment, the higher concentration of HMDSO and the lower concentration of MAA in the structure.

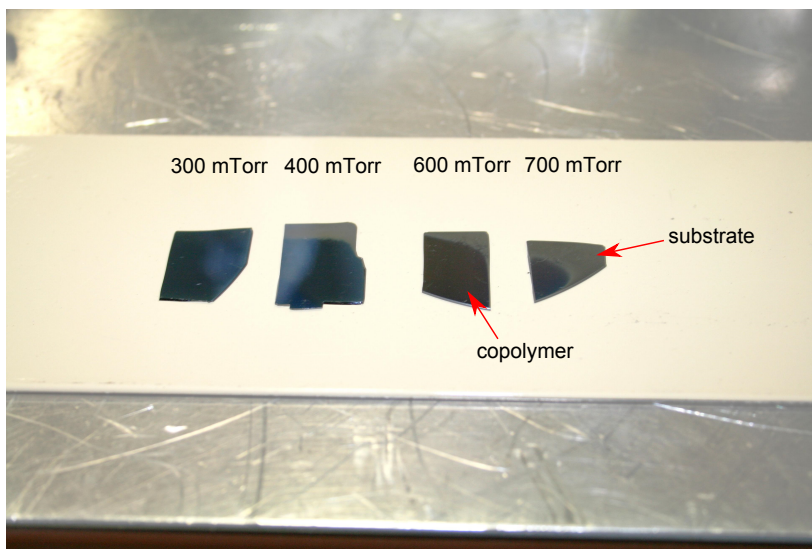


Figure 4.21: Stability in water after 1 hour at 20°C . The stability decreases as we increase the pressure.

4 Results and Discussion

4.2.7 Copolymer at constant HMDSO and varying MAA

This final series was deposited to investigate the proton conductivity of our films. In the previous depositions it was investigated how the system reacts to changes in various parameters. The goal of this series was to deposit films that are stable in water but still exhibit a proton conductive behavior. Therefore we chose the HMDSO flow rate to be 3 sccm (much hydrophobic material) and the pressure to be at 250 mTorr (high ion bombardment → high crosslinking). As the MAA was increased the films were checked for their stability in water. Since they became more unstable with higher flow rates of MAA the applied power was increased in an attempt to create a higher stability. The argon flow rate was chosen to be 4 sccm (higher deposition rate). The deposition parameters and the results of the conductivity measurements are shown in table 4.11.

The value for the resistance of the solution after the conductivity measurement are recorded because at higher resistance this value is needed to calculate the actual resistance of the membrane. The resistance of ultra pure water is 17.4 MΩ but this value is generally lowered due to degradation in the lab to around 270 kΩ. Additionally to the degradation of the water in the lab there will be a decrease of the resistance due to the dissolution of ions from the membrane during the measurement. Therefore looking at the resistance after the measurement is an indication how stable the films are. In table 4.11 one can see that the resistivity of the solution decreases up to Sample 147 although we would expect it to decrease for the whole series as the films got less stable in water. This is probably because we had to get new ultra pure water for the lab whose resistivity was probably a lot higher than the water which was in the lab before. As a comparison Nafion® exhibits immersed in water a resistivity of 265 Ω and the resistance of the solution after the membrane was measured

4.2 Copolymers

to be 289 kOhm which leads to a conductivity of around 100 mS. For the stable films we reach a conductivity of 1.1 mS which is substantially lower than the conductivity of Nafion®.

Table 4.11: Deposition parameters, deposition rate and results from the electrochemical impedance spectroscopy. R_{tot} is the total resistance of the membrane plus water and R_{sol} is the resistance of the water after the measurement with the membrane. The thickness was measured by profilometry.

Sample Number	144	145	146	147	148	149
MAA Flow / sccm	0.5	1	1.5	2	2.5	3
Power / W	30	30	30	35	40	45
Deposition rate / $\frac{nm}{min}$	25	45	64	70	68	67
R_{tot} / kOhm	202	138	75	38	55	65
R_{sol} / kOhm	252	237	225	123	204	241
Conductivity / $\frac{mS}{cm}$	1.1	1.5	3.4	10.4	5.2	5.6
Error / $\frac{mS}{cm}$	0.1	0.1	0.2	0.7	0.2	0.3

In figure 4.22 one can see the FTIR-spectra of the series. The changes in the chemical structure can be seen by the increasing C=O peak and the decreasing HMDSO peaks meaning that the copolymer with higher MAA flow rates also have more MAA in the structure.

A thickness measurement before and after water can be seen in table 4.12. These water stability tests in which the whole substrate is simply immersed in water for 10 minutes at 20 °C show that as the MAA content increases the films get more and more unstable in water. Since the films get more unstable the conductivity values for flow rates above 1.0 sccm should not be trusted but they are still reported in table 4.11.

4 Results and Discussion

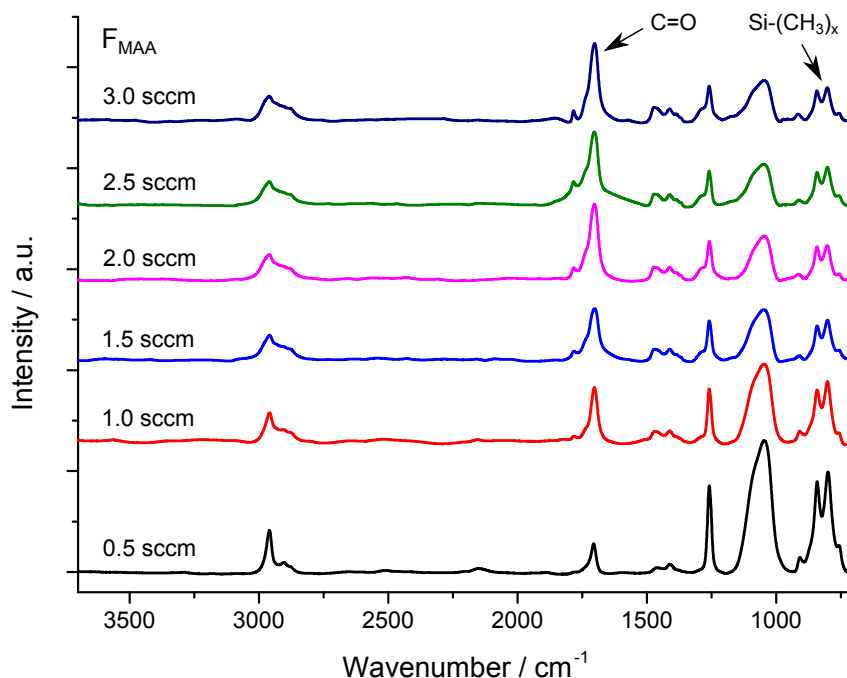


Figure 4.22: FTIR-spectra for a changing MAA flow rate. However investigating these spectra one needs to consider that the power is also varied at a certain point (see table 4.11). The x can stand for 3 or 2 corresponding to absorptions at 840 cm^{-1} and 800 cm^{-1} , respectively.

The conclusion that can be deduced from the water stability tests is that for this set of deposition parameters it is only possible to produce a stable structure if the amount of MAA is small compared to the HMDSO part. We can see from table 4.12 that actually only the deposition with the lowest MAA flow rate exhibits a swelling behavior and keeps its stability even after being immersed in water for one hour whereas the other depositions are dissolved after approximately half an hour. Also one can see that as the amount of MAA

4.2 Copolymers

in the sample increases the water stability seems to get worse.

Table 4.12: Thicknesses of the films before and after water treatment for 10 minutes at room temperature. As the MAA flow rate increases the stability in water reduces.

Sample Number	$F_{\text{MAA}} / \text{sccm}$	$d_{\text{before}} / \text{nm}$	$d_{\text{after}} / \text{nm}$	swelling / %
144	0.5	2620 ± 60	3006 ± 60	$+15 \pm 0.2$
145	1.0	5700 ± 210	5452 ± 120	-4 ± 0.2
146	1.5	8220 ± 330	7699 ± 160	-6 ± 0.3
147	2.0	5300 ± 160	4757 ± 170	-10 ± 0.3
148	2.5	6730 ± 190	5498 ± 70	-18 ± 0.2
149	3.0	5360 ± 20	4042 ± 80	-25 ± 0.2

Table 4.13: Water contact angles and conductivity values for the depositions that were stable enough in water to perform measurements.

$F_{\text{MAA}} / \text{sccm}$	$\phi_{\text{static}} / ^\circ$	$\phi_{\text{advancing}} / ^\circ$	$\phi_{\text{receding}} / ^\circ$	conductivity / $\frac{\text{mS}}{\text{cm}}$
0.5	105.4 ± 2	115.3 ± 0.5	98.5 ± 0.1	1.14
1	93.3 ± 1.6	135.2 ± 0.5	77.1 ± 0.1	1.50

In table 4.13 the water contact angles of the more stable depositions are shown. One can see that the small difference in the flow rate already has quite a big influence on the contact angles. The static contact angle is already significantly lower for the second deposition whereas the hysteresis is much larger.

5 Conclusion

Proton conductive polymers play an important role in the fuel cell industry. Since the current products provide still a potential to be improved it was the idea to develop a membrane that has a good proton conductivity and water stability at low production costs. As a depositing technique plasma enhanced chemical vapor deposition (PECVD) was used. PECVD has the advantages that it has a simple setup while it provides very homogeneous coatings and good stability due to crosslinking of the film. The choice of precursor is usually not an issue since the molecules are activated by the plasma.

With our system we are able to synthesize films of pure MAA and pure HMDSO or mixtures of these monomers. The deposition rate is strongly dependent on the parameters of the deposition such as the pressure, the power or the flow rates. After thoroughly investigating the changes in the chemical composition and the deposition rates of the monomers in the reactor it is fair to assume that the description of the system with the Yasuda factor is justified. The water contact angle measurements in section 4.2.2 show that our films exhibit a big hysteresis which leads us to the assumption that it is possible to achieve a high chain mobility in the copolymers. The variation of the argon flow rate showed only very little effect on the chemical composition whereas it did influence the deposition rate. From section 4.2.6 it can be deduced that the stability in water not only depends on the ratio of monomers and the Yasuda

5 Conclusion

factor but also depends on which pressure the films are deposited at. For lower pressure a higher ion bombardment of the sample is achieved which increases the crosslinking of the network and subsequently the stability in water which can be seen in figure 4.21. The electrochemical impedance spectroscopy results show that the produced polymers do indeed exhibit proton conductivity (conductivity around $1 \frac{\text{mS}}{\text{cm}}$) however the results for the majority of the data can not be trusted due to the lack of water stability. The stability in water turned out to be rather difficult to achieve with most of the depositions. Although some samples showed stability for a short time (20 min) most of them dissolved after being exposed for a longer time (60 min). Especially in the last series one can see in the FTIR-spectra for the deposition with a flow rate of 0.5 sccm one can see that the film is stable when the structure contains substantially more hydrophobic HMDSO groups than hydrophilic MAA groups. This leads us to the conclusion that it is possible to deposit proton conductive membranes that exhibit a swelling behavior (swelling of 15 %) when immersed in water if the ratio of HMDSO flow rate to MAA flow rate is sufficiently high and the films are deposited at a low pressure or when the Yasuda factor is high enough to incorporate mostly hydrophobic groups with the sacrifice of reducing the proton conductive groups.

Bibliography

1. F. Barbir. *PEM Fuel Cells: Theory and Practice* 537 pp. ISBN: 9780123877109 (Academic Press, 2013) (cit. on pp. 1, 3).
2. *Fuel Cell Vehicle* | TOYOTA GLOBAL SITE TOYOTA MOTOR CORPORATION GLOBAL WEBSITE. (2014) (cit. on p. 4).
3. J. Zhang, H. Zhang, J. Wu, and J. Zhang. in *Pem Fuel Cell Testing and Diagnosis* 143 (Elsevier, 2013). ISBN: 9780444536884. (Cit. on pp. 9, 10, 33).
4. T. Ogawa *et al.* "The proton conduction mechanism in a material consisting of packed acids." *Chem. Sci.* **5**, 4878. ISSN: 2041-6520, 2041-6539 (14, 2014) (cit. on p. 10).
5. A. Wohlfarth *et al.* "Proton Dissociation of Sulfonated Polysulfones: Influence of Molecular Structure and Conformation." *Macromolecules*. ISSN: 0024-9297. (5, 2015) (cit. on p. 10).
6. A. M. Coclite, P. Lund, R. Di Mundo, and F. Palumbo. "Novel hybrid fluoro-carboxylated copolymers deposited by initiated chemical vapor deposition as protonic membranes." *Polymer* **54**, 24. ISSN: 0032-3861 (8, 2013) (cit. on p. 10).

Bibliography

7. V. Neburchilov, J. Martin, H. Wang, and J. Zhang. "A review of polymer electrolyte membranes for direct methanol fuel cells." *Journal of Power Sources* **169**, 221. ISSN: 03787753 (2007) (cit. on pp. 10, 11).
8. S. J. Peighambardoust, S. Rowshanzamir, and M. Amjadi. "Review of the proton exchange membranes for fuel cell applications." *International Journal of Hydrogen Energy. The 1st Iranian Conference On Hydrogen & Fuel Cell* **35**, 9349. ISSN: 0360-3199 (2010) (cit. on pp. 10, 13).
9. R. Reeve. *Update on status of direct methanol fuel cells* (2002) (cit. on p. 12).
10. V. Neburchilov, J. Martin, H. Wang, and J. Zhang. "A review of polymer electrolyte membranes for direct methanol fuel cells." *Journal of Power Sources* **169**, 221. ISSN: 03787753 (2007) (cit. on p. 13).
11. L. Martinu, O. Zabeida, and J. E. Klemberg-Sapieha. in *Handbook of Deposition Technologies for Films and Coatings (Third Edition)* (ed P. M. Martin) 392 (William Andrew Publishing, Boston, 2010). ISBN: 978-0-8155-2031-3. (Cit. on pp. 14, 20).
12. R. d'Agostino, P. Favia, and F. Fracassi. *Plasma Processing of Polymers* 554 pp. ISBN: 9780792348597 (Springer Science & Business Media, 30, 1997) (cit. on p. 14).
13. C. R. Kleijn. "Transport phenomena in chemical vapor deposition reactors" (1991) (cit. on p. 14).
14. R. d'Agostino, F. Cramarossa, and S. De Benedictis. "Diagnostics and decomposition mechanism in radio-frequency discharges of fluorocarbons utilized for plasma etching or polymerization." *Plasma Chemistry and Plasma Processing* **2**, 213. ISSN: 0272-4324 (1982) (cit. on p. 18).

Bibliography

15. R. d'Agostino, F. Cramarossa, V. Colaprico, and R. d'Ettole. "Mechanisms of etching and polymerization in radiofrequency discharges of CF₄-H₂, CF₄-C₂F₄, C₂F₆-H₂, C₃F₈-H₂." *Journal of Applied Physics* **54**, 1284. ISSN: 0021-8979, 1089-7550 (1, 1983) (cit. on p. 18).
16. R. d'Agostino, F. Cramarossa, S. D. Benedictis, and G. Ferraro. "Spectroscopic diagnostics of CF₄-O₂ plasmas during Si and SiO₂ etching processes." *Journal of Applied Physics* **52**, 1259. ISSN: 0021-8979, 1089-7550 (1, 1981) (cit. on p. 18).
17. R. d'Agostino, S. D. Benedictis, and F. Cramarossa. "Radiofrequency plasma decomposition of C_nF_{2n+2}-H₂ and CF₄-C₂F₄ mixtures during Si etching or fluoropolymer deposition." *Plasma Chemistry and Plasma Processing* **4**, 1. ISSN: 0272-4324, 1572-8986 (1, 1984) (cit. on p. 18).
18. R. d'Agostino, F. Cramarossa, and S. D. Benedictis. "Chemical mechanisms in C₃F₈-H₂ radiofrequency discharges." *Plasma Chemistry and Plasma Processing* **4**, 21. ISSN: 0272-4324, 1572-8986 (1, 1984) (cit. on p. 18).
19. R. d'Agostino, V. Colaprico, and F. Cramarossa. "The use of "actinometer" gases in optical diagnostics of plasma etching mixtures: SF₆-O₂." *Plasma Chemistry and Plasma Processing* **1**, 365. ISSN: 0272-4324, 1572-8986 (1, 1981) (cit. on p. 18).
20. H. Yasuda and T. Hirotsu. "Critical evaluation of conditions of plasma polymerization." *Journal of Polymer Science: Polymer Chemistry Edition* **16**, 743 (1978) (cit. on p. 19).
21. D. Hegemann. "Influence of pressure on an asymmetric, radio frequency discharge with methane." *Thin Solid Films* **515**, 2173 (2006) (cit. on p. 20).

Bibliography

22. D. Hegemann and M.-M. Hossain. "Influence of Non-Polymerizable Gases Added During Plasma Polymerization." *Plasma Processes and Polymers* **2**, 554 (2005) (cit. on pp. 20, 55, 56).
23. E. Riedel. *Allgemeine und Anorganische Chemie* ISBN: 978-3-11-022782-6. (De Gruyter, Berlin, Boston, 2010) (cit. on p. 23).
24. P. Larkin. in *Infrared and Raman Spectroscopy* (ed P. Larkin) 7 (Elsevier, Oxford, 2011). ISBN: 978-0-12-386984-5. (Cit. on p. 25).
25. C. Rau and W. Kulisch. "Mechanisms of plasma polymerization of various silico-organic monomers." *Thin Solid Films* **249**, 28. ISSN: 0040-6090 (1, 1994) (cit. on p. 28).
26. A. Grill and D. A. Neumayer. "Structure of low dielectric constant to extreme low dielectric constant SiCOH films: Fourier transform infrared spectroscopy characterization." *Journal of Applied Physics* **94**, 6697. ISSN: 0021-8979, 1089-7550 (15, 2003) (cit. on p. 28).
27. G. Socrates. *Infrared and Raman Characteristic Group Frequencies: Tables and Charts* 372 pp. ISBN: 9780470093078 (John Wiley & Sons, 18, 2004) (cit. on p. 28).
28. M. Birkholz. *Thin film analysis by X-ray scattering XXII*, 356. ISBN: 9783527310524. (Wiley-VCH, Weinheim, 2006) (cit. on p. 29).
29. Y. Yuan and T. R. Lee. in *Surface Science Techniques* (eds G. Bracco and B. Holst) *Springer Series in Surface Sciences* 51, 3 (Springer Berlin Heidelberg, 1, 2013). ISBN: 978-3-642-34242-4, 978-3-642-34243-1. (Cit. on p. 32).

Bibliography

30. H. Yasuda, A. K. Sharma, and T. Yasuda. "Effect of orientation and mobility of polymer molecules at surfaces on contact angle and its hysteresis." *Journal of Polymer Science: Polymer Physics Edition* **19**, 1285. ISSN: 1542-9385 (1981) (cit. on p. 33).
31. K. C. Emma Dedmond. "Application Note - Effect of Solution Conductivity on In-Plane Membrane Conductivity Measurement." *Scribner Associates, Inc.* (Cit. on p. 34).